13(1)

気象庁欧文海洋報告

第13巻 第1号

THE OCEANOGRAPHICAL MAGAZINE

Vol. 13 No. 1

LIBRARY
APR 9 1962
FISH & WILDLIFE SERVICE

CONTENTS

M. Tsuchiya: An oceanographic description of the Equatorial Current System of the Western Pacific 1

S. Konaga: Kuroshio in Enshū-nada—Variations of the depth of isotherms 31

M. Yasui, J. Masuzawa, T. Sawara and T. Nakai: Soundings of the Ramapo Deep 41

M. Miyazaki, T. Ueno and S. Unoki: Theoretical investigations of typhoon surges along the Japanese coast 51

Published by the Japan Meteorological Agency

October 1961

The Oceanographical Magazine
Vol. 13. No. 1, October 1961

An Oceanographic Description of the Equatorial Current System of the Western Pacific

By

Mizuki TSUCHIYA

Meteorological College, JMA

(Received May 1, 1961)

1. *Introduction*

In recent ten years, many systematic and extensive oceanographic observations have been carried out in the Eastern Equatorial Pacific, and our understanding of the oceanographic features in this region is making rapid progress. The most striking result of these observations is the discovery of the Equatorial Undercurrent or the *Cromwell Current* whose existence no one suspected ten years ago. These observations are, however, confined to the eastern half of the Pacific with an exception, an international joint expedition EquaPac, which covers the entire equatorial waters of the Pacific.

On the contrary to the active studies of the Eastern Equatorial Pacific, recent observations in the western part are quite few and we have only several cruises of Shyunkotsu-maru, Expedition EquaPac, direct current measurements made aboard Takuyo and Satsuma in the IGY, and some other cruises of a few fisheries research vessels. These observations other than EquaPac and IGY project were planned for each particular purpose, such as investigation of radiological contamination of sea water due to the nuclear test explosions or exploration of fishing grounds. Such surveys, therefore, can not always be useful from the oceanographic point of view, although they serve their own particular purposes. In this circumstance, it is desirable to have some systematic and comprehensive observations in the Western Equatorial Pacific in order to know more detailed oceanographic features in this region which are supposed to be in a close correlation with those in the eastern part. Without such new carefully planned observations, it would be impossible to completely understand the oceanography of the entire Equatorial Pacific.

Fortunately, this desire is, to some extent, satisfied with the oceanographic data obtained before the World War II. The survey vessels of the Japanese Navy Hydrographic Department had made many oceanographic observations in the entire Northwestern Pacific since 1923 until the War obliged us to give up these series of observations. Some parts of these data were obtained in the equatorial waters and were partly used by several investigators in their studies, but most of them remain untouched. If one deals with these data in an adequate manner, they would increase our information of the oceanographic features of the Western Equatorial Pacific to some degree, but of course a limitation is expected unless some new systematic observations are made in future.

In this situation, by the use of these data hitherto unused, the author presents an oceanographic description of the Equatorial Current System of the Western Pacific in order to fulfil insufficient observations of the present time and also to give a basis of the planning for the future observations.

In several of the earlier cruises of these surveys, the observations were confined only to temperature in upper 500 meters and its accuracy is not so high as in the later cruises. In later ones, temperature and salinity values with a sufficient accuracy were obtained by a number of hydrographic casts which reached down to 1000 meters at most stations and down to 1500 meters or more at the other stations. In addition to these hydrographic casts, direct measurements of currents with Ekman's current meters were also made at a considerable number of stations. Some of these observations extending over more than fifteen years are fragmentary both in spatial distribution of the occupied stations and in time interval of each observation. Therefore, these data must be processed with special care, and those which can not be used for any purpose in the present study are omitted from the analysis.

The data used in the present study are taken from the publications* of the Hydrographic Office, Japan Maritime Safety Board (1933, 1950–1952) and summarized in the following table.

The present analysis of the current system essentially depends on the geostrophic balance of Coriolis' force and the pressure gradient in the sea, because the geostrophic balance is supposed to be encountered in the actual ocean with

* In these publications, only interpolated values of temperature and salinity are tabulated. Therefore, in the present study these interpolated values are used to construct temperature or salinity sections instead of using the observed values.

a good approximation even in low latitude region where the Coriolis parameter is very small. But in the surface layers which are affected by the stresses due to the wind over the sea, the actual current would be more or less modified from the geostrophically computed one. And further, short period motions of local character such as internal waves, which alter the mass distribution largely, would not be reflected in the goestrophic current. Therefore the result must be interpreted carefully.

2. *The Equatorial Current System of the Pacific*

The Equatorial Current System of the Pacific has been considered to consist of the North and South Equatorial Currents, and the Equatorial Counter-

Table 1. List of oceanographic observations in the Western Equatorial Pacific used in the present study.

Cruise No.	Ship	Year	Month	Area of Observation	
				Western and Eastern Limits of Observation	Southern Limit of Observation
—	Mansyu	1925 1926	Sept.-Oct. May, Oct.	127°-162°E	0°
—	Mansyu	1927-28	Nov.-Mar.	140°-170°E	0°
16	Kosyu	1931	Oct.	173°E	2°N
19	Kosyu	1932	May	163.5°E	1°N
27	Kosyu	1933	Apr.-May Aug.-Oct.	131°-156°E	0°
31	Komahasi	1934-35	Nov.-Mar.	126°-145°E	0°
32	Kosyu	1934-35	June-Feb.	135°-175°E	1°S
34	Komahasi	1936	Jan.-Mar.	146°-157°E	7°N
35	Katuriki	1935-36	Nov.-Feb.	126°-157°E	0°
36	Kosyu	1935	May-Oct.	159°-175°E	1°S
42	Kosyu	1936	Apr.-Oct.	135°-168°E	3°S
43	Kosyu	1936-37	Dec.-Feb.	146°-170°E	0°
48	Kosyu	1937	Apr.-Sept.	127°-158°E	1°N
52	Kosyu	1938	Apr.-July	125°-158°E	1°S
67	Katuriki	1940	July-Dec.	142°-175°E	1°N
68	Komahasi	1941	Apr.-May	127°-135°E	1°N
69	Komahasi	1941	May-June	132°-153°E	1°S
70	Komahasi	1941	June	133°-151°E	8°N
72	Komahasi	1941	Sept.	146°-163°E	8°N
73	Komahasi	1941	Sept.-Oct.	156°-171°E	4°S
74	Komahasi	1941	Oct.-Nov.	155°E-180°	0°

current imbedded between them. To these three currents described in standard text-books of oceanography, we must add the Equatorial Undercurrent or the *Cromwell Current* and the South Equatorial Countercurrent both of which were recently revealed in the Equatorial Pacific.

The Equatorial Undercurrent was first discovered by CROMWELL, MONTGOMERY, and STROUP in 1952 (CROMWELL *et al.*, 1954) and its detailed structure was measured by KNAUSS (1960). The characteristic features of this current are as follows: It exists in the narrow equatorial belt between 2° S and 2° N and has a symmetrical structure about the equator. Its maximum velocity is about 120–150 cm/sec towards the east and is found in the depth of about 100 meters at 140° W and about 50 meters at 95° W with a slope of about 1.3×10^{-5}. The thickness of the current is about 400 meters between the depths of 50 and 500 meters. This current is revealed between 150° W and 92° W and it disappears abruptly at 89° W to the east of the Galapagos Islands. Time variation both in current speed and current axis is quite small and this current seems to be almost steady, while the other ocean currents show marked variations.

The evidence of the South Equatorial Countercurrent, which flows towards the east just in the symmetrical latitudes of the southern hemisphere with the Equatorial Countercurrent about the equator, was presented by REID (1959). Therefore, if it is established, what has so far been called the Equatorial Countercurrent should be called more properly the North Equatorial Countercurrent and the westward current between these two Countercurrents which has been thought to be the northern edge of the South Equatorial Current should be called with another appropriate name.

In this study, therefore, particular attention is paid to the existence of the South Equatorial Countercurrent and the Equatorial Undercurrent; however the complete lack of the observational data in the southern hemisphere did not allow me to examine the existence of the South Equatorial Countercurrent in the Western Pacific. Hence the names of the Equatorial Countercurrent and the South Equatorial Current, which are in common use, are used in the present study to avoid confusion.

Owing to the scarcity of the observational data to the south of the equator, the description of the South Equatorial Current given here is not so much. Therefore, the chief subject of this study is confined to the Equatorial Counter-

current and Undercurrent, the North Equatorial Current being placed out of the scope of the present work.

3. The Equatorial Countercurrent

In this section, the description of the Equatorial Countercurrent in view of the temperature distribution and the dynamic topography will be presented.

For this purpose, all the possible dynamic topography charts, dynamic sections as well as temperature sections are constructed. The dynamic topography charts referred to the 1000 db surface, which are constructed in this study, should be understood as representing some average conditions during the period of a month or two, within which the observations had been made. The spacing of the stations is irregular but generally speaking they were occupied at a distance of about 1° in the north-south direction and about 500 kilometers in the east-west direction. Therefore discussions are confined to the features with zonal scales larger than some hundreds kilometers, and consequently the contouring is made with reference to this scale. On the other hand, the sections should be interpreted as representing some average conditions during the period of about ten days within which the observations had been made in general cases.

Some examples of the temperature and the dynamic sections are illustrated in Figs. 1–14. In these figures, the Equatorial Countercurrent is revealed by the deepening of the thermocline or the rising of the isobaric surfaces towards the equator which begins at about 8° N and terminates at about 3° N on the average. So far as these sections illustrated here and the other dynamic sections and topographic charts, which represent the average conditions in the different months of the different years, are concerned, the Equatorial Coutercurrent identified with the upward slope of the isobaric surfaces and downward slope of the thermocline towards the equator is always present, except the section along 155° E meridian in Sept., 1933, in which no definite indication of the Countercurrent is found in the dynamic section between the equator and 15° N, while a slight downward slope of the thermocline towards the equator is found between about 3° N and 7° N in the temperature section. According to WYRTKI (1957), to the north of the New Guinea Island the Equatorial Countercurrent disappears in April and the westward current is predominant all around there, but because of the complete lack of the obser-

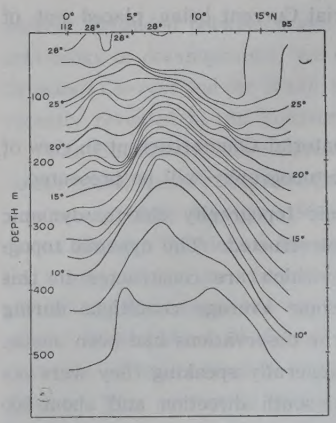

Fig. 1. Temperature section along 136.5°E. *Komahasi*, Cruise 31, Sts. 95–112. Feb., 1935.

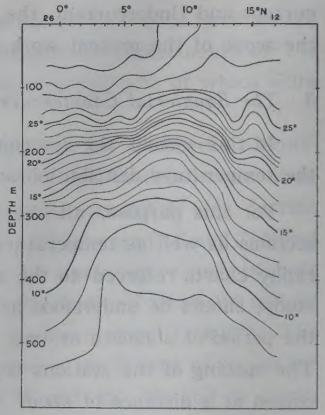

Fig. 2. Temperature section approximately along 135°E. *Kosyu*, Cruise 42, Sts. 12–26. Apr.–May, 1936.

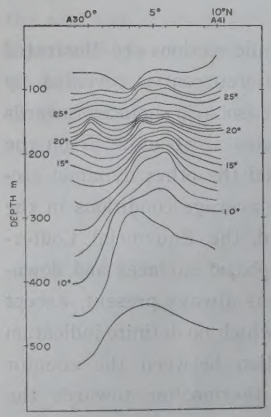

Fig. 3. Temperature section approximately along 140°E. *Kosyu*, Cruise 32, Sts. A30–A41. June–July, 1934.

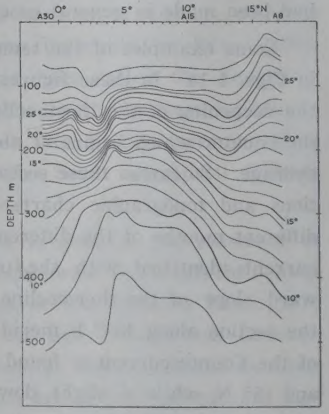

Fig. 4. Temperature section along 142°E. *Kosyu*, Cruise 32, Sts. A8–A30. July, Sept., 1934.

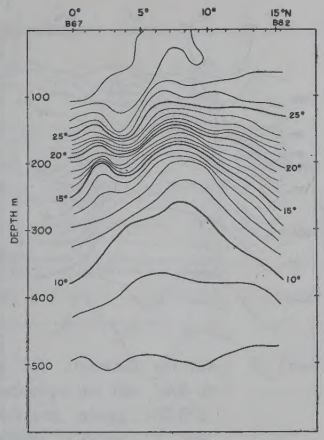

Fig. 5. Temperature section along 156°E. *Kosyu*, Cruise 32, Sts. B67–B82. Feb., 1935.

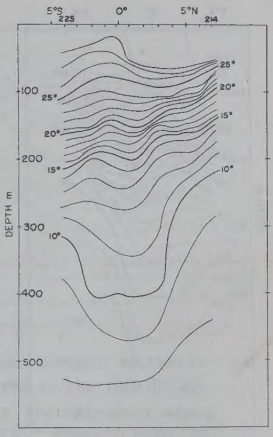

Fig. 6. Temperature section approximately along 157°E. *Komahasi*, Cruise 73, Sts. 214–225. Sept., 1941.

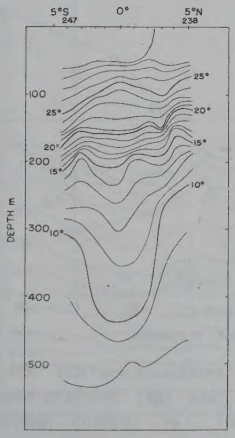

Fig. 7. Temperature section approximately along 166°E. *Komahasi*, Cruise 73, Sts. 238–247. Oct., 1941.

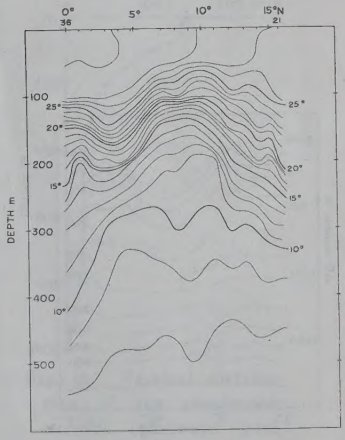

Fig. 8. Temperature section approximately along 169°E. *Kosyu*, Cruise 43, Sts. 21–36. Dec., 1936–Jan., 1937.

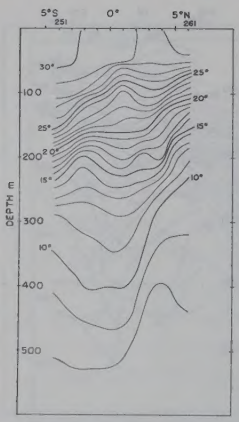

Fig. 9. Temperature section approximately along 170°E. *Komahasi*, Cruise 73–74, Sts. 251–261. Oct., 1941.

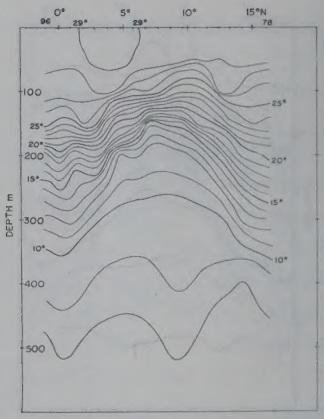

Fig. 10. Temperature section approximately along 174°E. *Kosyu*, Cruise 36, Sts. 78–96. Aug., 1935.

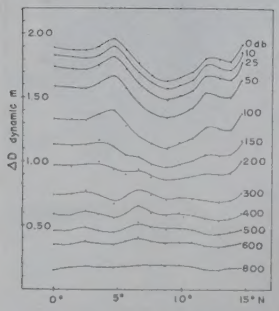

Fig. 11. Dynamic section referred to the 1000 db surface approximately along 137°E. *Katuriki*, Cruise 36, Sts. 66-80. Jan., 1936.

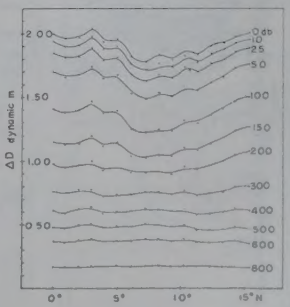

Fig. 12. Dynamic section referred to the 1000 db surface along 156°E. *Kosyu*, Cruise 32, Sts. B67–B82. Feb., 1935.

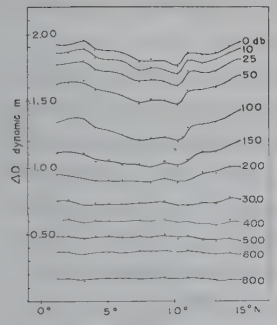

Fig. 13. Dynamic section referred to the 1000 db surface along 163.5°E. *Kosyu*, Cruise 32, Sts. B37-B51. Jan., 1935.

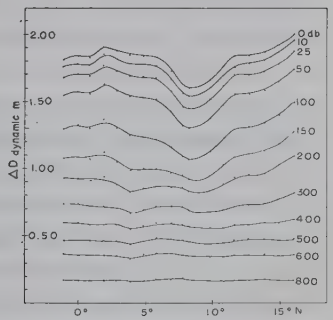

Fig. 14. Dynamic section referred to the 1000 db surface approximately along 172°E. *Kosyu*, Cruise 36, Sts. 70-76, 97-107. Aug., 1935.

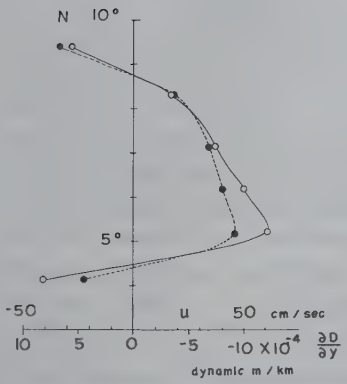

Fig. 15. Surface meridional pressure gradient (●) and geostrophic current (○) in the Equatorial Countercurrent along 137°E section. *Kosyu*, Cruise 35, Sts. 71-77. Jan., 1936. The pressure gradient is positive to the north and the current positive to the east.

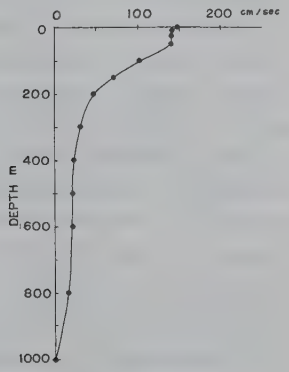

Fig. 16. Vertical distribution of the geostrophic current (eastward positive) in the Equatorial Countercurrent. 178°E, 4.5°N. *Komahasi*, Cruise 74, Sts. 275-276. Oct., 1941.

vational data in this region in April, neither positive nor negative conclusions to his result are obtained here.

From these dynamic sections, nine sections which are the closest to being exactly meridional were selected for the geostrophic computation of the east-west component of the Equatorial Countercurrent. As an example, the profile of the surface geostrophic current across the section along 137° E meridian is shown in Fig. 15. A characteristic feature of this profile is a smaller shear in the northern side and a larger shear in the southern side of the Countercurrent. This is partly due to the larger pressure gradient (broken line in the figure) and partly due to the smaller Coriolis parameter in the southern side of the Countercurrent because in this latitude the variation of the Coriolis parameter with latitude is very large. In most of the other sections, although they are not illustrated here, maximum velocities of about 50–150 cm/sec are found more or less in the southern half of the Equatorial Countercurrent.

The vertical profile of the geostrophic current in the Equatorial Countercurrent at about 178° E, 4.5° N in Oct., 1941 is also shown in Fig. 16 as a typical example. As seen in the figure, although larger speed is confined to the upper 200 meters, a speed of about 20 cm/sec is still appreciable below 400 meters. At some other stations, the maximum speed is found at a depth of about 25 meters and the surface current is a little less than the maximum speed. This subsurface maximum is related to the surface low salinity layer in the northern half of the Equatorial Countercurrent because there is no temperature gradient in the surface layer to compensate the observed salinity gradient. A detailed discussion of such a subsurface maximum of the geostrophic current is, however, of not much significance, because the stresses due to the wind greatly modify the geostrophic current in such a shallow surface layer.

It is evident in the temperature and the dynamic sections that the Equatorial Countercurrent extends southward beneath the surface, whereas there is no subsurface northward extension of the Countercurrent. As seen in Figs. 13 and 14, the maximum height of the isobaric surfaces in the dynamic sections which indicates the southern boundary of the Equatorial Countercurrent is displaced equator-wards as the depth increases, more frequently in the western ones. A detailed discussion is very difficult because of the small gradient of the isobaric surfaces near the equator, but this feature is also

evident in the sections which are not illustrated here. Further discussion will be given in the next section in connection with the Equatorial Undercurrent in the Western Pacific.

Another interesting feature worthy of mention is the westward current which is often found below the eastward current between the depth of about 200 and 600 meters. For example, in Figs. 11 and 14 the downward slope of the isobaric surfaces of 200-600 db towards the equator is clearly seen between 5° N and 7° N. This is undoubtedly related to the intrusion of the intermediate water of the North Pacific characterized by the salinity minimum.

The total net eastward transport of the Equatorial Countercurrent over the 1000 db surface is computed for each section and tabulated in Table 2. Although the Equatorial Countercurrent extends to the south in the subsurface layer, the computation is made between the northern and southern boundaries of the Countercurrent at the surface. The transport due to the subsurface westward current just mentioned above is, if it is present, subtracted.

The computed transport shows considerable variations, but we can not get any definite idea on these variations, whether they are time variations or longitudinal ones. Nevertheless, it seems that the Equatorial Countercurrent is subjected to the variations of considerably small scale or of considerably short period. As shown in Table 2, the transport across the 138° E section in June—July, 1934 has an extremely small value of 9×10^6 m³/sec, while that across 142° E section in July, 1934 is 47×10^6 m³/sec. Within a distance of about 400 kilometers and within a time interval of about twenty days, it increases

Table 2. Total net eastward transport of the Equatorial Countercurrent over the 1000 db surface.

Long.	Stations	Month and Year	Transport
136.5°E	Komahasi 31, 105-109	Feb., 1935	48×10^6 m³/sec
137°	Katuriki 35, 72-96	Jan., 1936	30
138°	Kosyu 32, A44-A49	June-July, 1934	9
142°	Kosyu 32, A32-A27	July, 1934	47
156°	Kosyu 32, B70-B74	Feb., 1935	31
163.5°	Kosyu 32, B39-B46	Jan., 1935	12
171°	Kosyu 36, 100-107	Aug., 1935	39
173°	Kosyu 36, 86-92	Aug., 1935	32
178°	Komahasi 74, 274-278	Oct., 1941	61

about five times. It must be, however, borne in mind that thus computed transport severely depends on the choice of the reference level.

With regard to the time variation of the Equatorial Countercurrent we can not discuss whether they are seasonal ones or ones of shorter periods, so far as the present insufficient data are concerned. However, it shows considerable variations in both the strength and the location, just as revealed by Austin, Stroup, and Rinkel (1956), Knauss and Pepin (1959), and Knauss (1961) in the Eastern Pacific. The northern boundary (thin lines) and the southern boundary (thick lines) of the Countercurrent in the period of 1933–1941 are determined based on the dynamic topography and on direct current measurements and are shown in Fig. 17. One the average, the Countercurrent exists between 3° N and 8° N but fluctuates to north and south with a range of more than 3° in latitude. The meandering pattern of the Countercurrent is one of the interesting features. Since the stations are widely spaced in the longitudinal direction as already mentioned, a continuous line in the figure indicating the boundary of the Countercurrent would be also interpreted as a smoothed line of a train of many eddies. This would be a quite possible interpretation. A discussion from such a view point is, however, not warranted on the basis of the present data.

4. *The Equatorial Undercurrent*

The existence of the Equatorial Undercurrent has been established between 150° W and 92° W, but we have had no definite evidence of the westward ex-

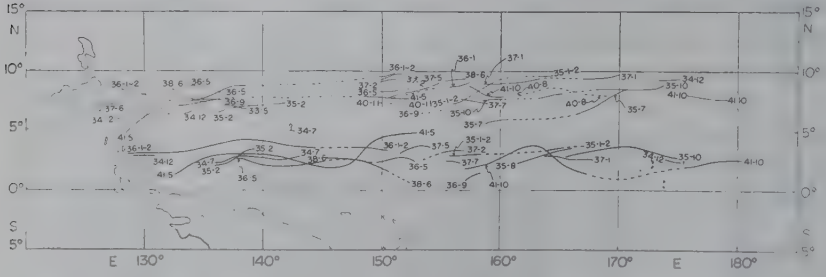

Fig. 17. Northern boundary (thin lines) and southern boundary (thick lines) of the Equatorial Countercurrent as inferred from the dynamic topography and the direct measurements in the period 1933–1941. The numerals indicate the year and the month. For example, 35-2 means Feb., 1935.

tension of the Undercurrent. Hence, it is of particular interest to investigate whether or not the Undercurrent is also present in the Western Pacific. For this purpose, direct measurements of the currents at and near the equator were carried out aboard Takuyo and Satsuma along several meridional sections between 147° and 157° E in Jan.—Feb., 1958 (Yoshida, Nitani, and Suzuki, 1959). The result of this observation is not so clear as in the eastern part because of fairly rapid variation of the current conditions during the period of the observation. But it suggests a subsurface eastward current below the surface westward current and this eastward current seems continuous with the Equatorial Countercurrent to the north of it, whereas the Undercurrent in the Eastern Pacific is clearly separated from the Countercurrent.

To get clear and more detailed feature in the Western Pacific, new observations just as made by Cromwell et al. and Knauss would be indispensable. However, in the light of the past data, some evidences of an eastward subsurface current at and near the equator are obtained in the Western Pacific.

In meridional or approximately meridional temperature sections illustrated in Figs. 1–10, the isotherms in the lower part of the thermocline layer between the depth of about 200 and 400 meters slope down towards the equator from about 5° N and 5° S with nearly symmetrical pattern about the equator, however most sections are confined to the north of the equator; those which cross the equator to the southern hemisphere are quite few. For example, the 10°C-isotherm increases its depth about 100 meters from a depth of 300 meters at 5° N to a depth of 400 meters at the equator. This deepening of the isotherms in the lower part of the thermocline layer creates a fairly homogeneous layer between the depth of about 200 and 400 meters. This characteristic feature near the equator is revealed more or less in every section between 130° E and 175° E.

The same feature with more pronounced structure is quite common in the Eastern Pacific and its close correlation with the Equatorial Undercurrent is discussed by Yoshida (1959). Some differences are, however, found between these features in the Eastern and Western Pacific. First, in the Eastern Pacific the isotherms in the upper part of the thermocline layer bend upwards between about 2° N and 2° S indicating the intense upwelling at the equator, while no such a conspicuous upward bend of the isotherms is revealed in the Western Pacific. Secondly, in the Eastern Pacific the homogeneous layer in

the thermocline extends between 2° N and 2° S with much smaller horizontal scale than in the west. Thirdly, the core depth of the homogeneous layer is about 100 meters or less in the Eastern Pacific, while it is found at the appreciably deeper depth of about 250 meters in the west. Finally, in the Eastern Pacific the thermocline slopes down to the south in the Equatorial Countercurrent region and reaches a maximum depth at about 4° N or so, where it turns to an upward slope towards the equator indicating the southern boundary of the Countercurrent. At about 2° N the isotherms in the upper part show a conspicuous upward bend and those in the lower part a conspicuous downward bend. While in the Western Pacific, the thermocline reaches a maximum depth at about 4° N or so and then turns to a gentle upward slope towards the equator just as in the east. The lower isotherms, however, continue to slope down towards the equator instead of turning to the upward slope together with the upper isotherms and create the homogeneous layer between the depth of about 200 and 400 meters as mentioned above. This seems to indicate that the Equatorial Countercurrent in the Western Pacific extends towards the equator in the subsurface layer.

The existence of this homogeneous layer in the intermediate depth at the equator may be interpreted to indicate the existence of an eastward subsurface current at the equator. As the geostrophic balance is a good approximation even in the low latitude as shown by Tsuchiya (1955) and by Knauss (1960), this eastward current will be able to be verified in a somewhat quantitative manner. It is, however, very difficult to estimate the eastward current near the equator by the geostrophic computation, because a small difference of dynamic height of a isobaric surface corresponds to a very large current speed in the low latitude region of the present interest, where the Coriolis parameter is vanishingly small. Moreover, as will be seen in Fig. 1-14, the temperature sections and consequently the dynamic sections often show small scale fluctuations of isotherms or isobars which might be due to some local disturbances of shorter periods or might be observational errors. In this circumstance, the interpretation of the geostrophically computed current in each separate section prepared by the use of the present data is quite difficult, or in more straightforward speaking, almost impossible.

Therefore, in the present analysis the equatorial waters of the Western Pacific are divided into four regions each between 130° and 140° E, 140° and

150° E, 150° and 160° E, and 160° and 175° E. In each region, all possible pairs of hydrographic stations, which are occupied approximately on the same meridian one near the equator and the other near 3° N, are selected from the cruises tabulated in Table 1. The number of thus selected pairs of stations in each region is tabulated in Table 3. These stations include observations in the different seasons of the different years, but the difference of the time of the observation at two stations of each pair does not exceed two days.

Table 3. The number of pairs of stations in each region used in the analysis of the Equatorial Undercurrent in the Western Pacific.

Region	130°–140°E	140°–150°E	150°–160°E	160°–175°E
Number of pairs of stations	13	12	10	9

The difference of the observed thermosteric anomaly (Δst) of a pair of stations is computed for each pair and plotted against the depth as shown in Figs. 18–21. For the pair in which a station deviates from the equator or 3°N considerably the computed difference is reduced to the value corresponding to the distance of 3° in latitude by linear extrapolation or interpolation. The plotted points scatter considerably especially in the upper 200 meters, nevertheless less dense water with larger thermosteric anomaly than the northern water on the same level, corresponding to the homogeneous layer in the thermocline, is clearly seen between the depth of 200 meters and 400 meters in the eastern regions, while it is obscure in the western regions. The situation becomes clearer by averaging the difference of the thermosteric anomaly at each depth. These averaged values are plotted against the depth in the same manner in Figs. 22–25. By integrating the averaged differences of the thermosteric anomaly, the average dynamic height difference between the equator and 3° N will be readily obtained. In this process, the contribution of the pressure terms is small and can be safely neglected. But this process implies the uncertainty of the reference level and also the uncertainty of small difference of the thermosteric anomaly in deeper layers whose significance is supposed to be still less even after the averaging process.

Therefore, models of the thermosteric anomaly difference, in which it vanishes below 600 meters, are adopted as shown in Figs. 22–25. The assumed models are somewhat arbitrary in the upper 100 meters, but they are less significant in those layers due to the larger scatter of the plotted points, and

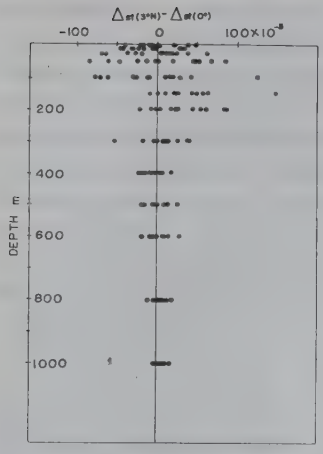

Fig. 18. Difference of the thermosteric anomaly between the equator and 3°N in the region between 130° and 140°E.

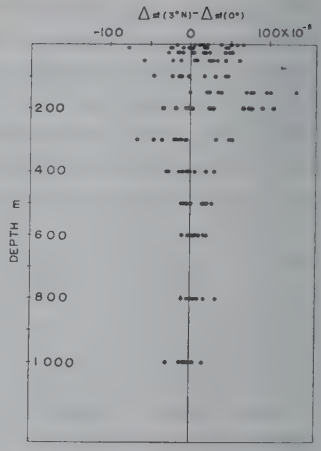

Fig. 19. Difference of the thermosteric anomaly between the equator and 3°N in the region between 140° and 150°E.

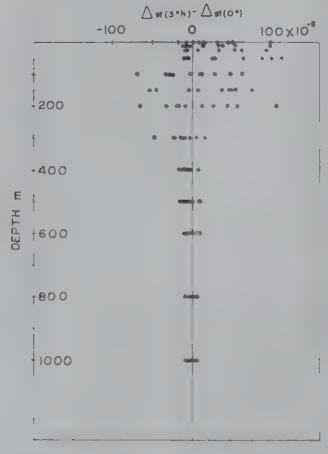

Fig. 20. Difference of the thermosteric anomaly between the equator and 3°N in the region between 150° and 160°E.

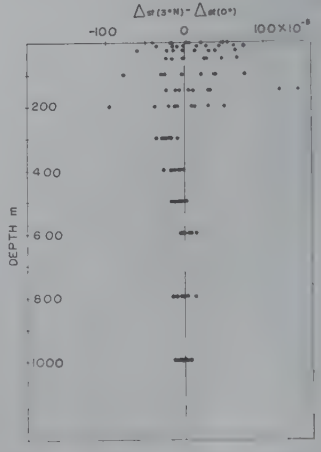

Fig. 21. Difference of the thermosteric anomaly between the equator and 3°N in the region between 160° and 175°E.

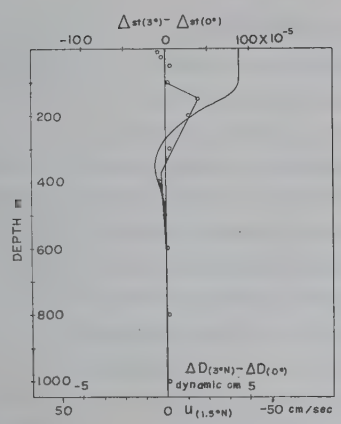

Fig. 22. Average difference of the thermosteric anomaly between the equator and 3°N (○) and its model assumed for the dynamic computation in the region between 130° and 140°E. The average pressure gradient or the corresponding east-west component (eastward positive) of the geostrophic current at 1.5°N is also shown.

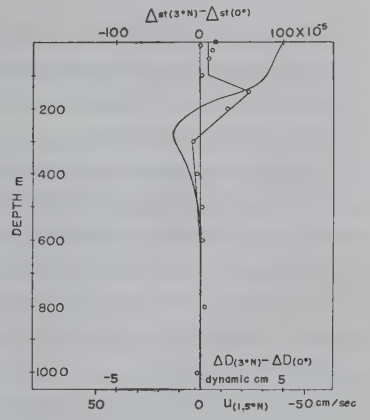

Fig. 23. Average difference of the thermosteric anomaly between the equator and 3°N (○) and its model assumed for the dynamic computation in the region between 140° and 150°E. The average pressure gradient or the corresponding east-west component (eastward positive) of the geostrophic current at 1.5°N is also shown.

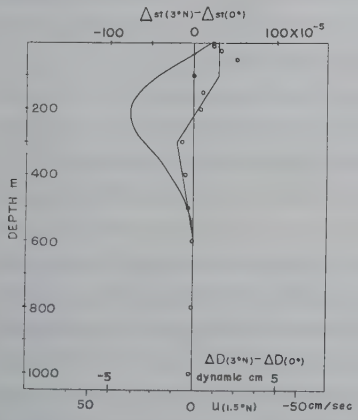

Fig. 24. Average difference of the thermosteric anomaly between the equator and 3°N (○) and its model assumed for the dynamic computation in the region between 150° and 160°E. The average pressure gradient or the corresponding east-west component (eastward positive) of the geostrophic current at 1.5°N is also shown.

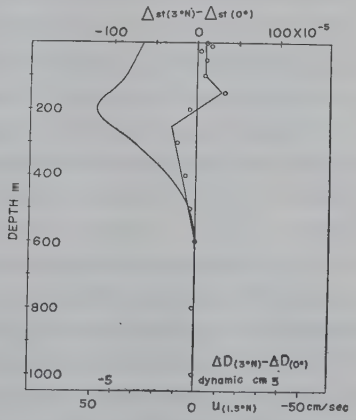

Fig. 25. Average difference of the thermosteric anomaly between the equator and 3°N (○) and its model assumed for the dynamic computation in the region between 160° and 175°E. The average pressure gradient or the corresponding east-west component (eastward positive) of the geostrophic current at 1.5°N is also shown.

further, as mentiond before, the stresses due to wind would be predominant in those layers and hence the computed current can not be directly interpreted as an actual one. Therefore this arbitrariness in the models is not essential to the present discussions.

Thus computed dynamic height differences between the equator and 3°N are also shown in Figs. 22–25 ($\Delta D_{(3°N)}-\Delta D_{(0°)}$ in the figures). If one assumes that the pressure gradient corresponding to this dynamic height difference is present at 1.5°N, the middle latitude between the equator and 3°N, a difference of 5 dynamic centimeters is equivalent to the eastwest component of the current velocity of about 40 cm/sec as indicated by the scale at the bottom of the figures.

As seen in Figs. 22–25, an eastward current with its maximum speed at 200 meters in the 160°–175°E region and with a little weaker maximum speed at 220 meters in the 150°–160°E region is clearly revealed. In the 140°–150°E region, a much weaker eastward current is found at 280 meters but its reality is out side of the accuracy of the present discussions. In the 130°–140°E region, the eastward current should be regarded as missing with the present accuracy. The core depth of this eastward current seems to become deeper towards the west but this sharply depends on the assumed models of the thermosteric anomaly, therefore such a discussion has not much significance.

It would be interesting to remark that the extrapolation of the average longitudinal slope of the core depth 1.3×10^{-5}, which was measured by KNAUSS in the Equatorial Undercurrent of the Eastern Pacific, to the Western Pacific gives a depth of 190 meters at 160°E, just the same depth obtained here.

As already mentioned, an inference that this eastward current seems continuous with the Equatorial Countercurrent is drawn from the temperature sections. This is also seen in the dynamic sections as the gentle upward slope of the isobars of 150–300 db towards the equator (Figs. 13 and 14). But due to the small slope of the isobars near the equator, detailed discussions are impossible. Nevertheless, it seems that the slopes are frequently found in the sections to the east of about 150°E and scarcely in the western sections, although most of the prepared sections are not illustrated here. More detailed features can not be deduced from the data presently at hand. With regard to the southern limit of the eastward current, only an inference that it may extend to

about 4°S or so can be drawn from a few temperature sections across the equator (Figs. 6, 7, and 9).

If we tentatively assume that the above computed eastward current is uniformly distributed between 3°N and 3°S, the total eastward transport of this current is about 90×10^6 m³/sec in the 160–175°E region and 55×10^6 m³/sec is the 150°–160°E region. It would be, however, of not much significance to compare these rough order-of-magnitude estimations with the value of 39×10^6 m³/sec directly measured by KNAUSS at 140°W.

On the other hand, direct measurements of currents with Ekman's current meters were made at a considerable number of stations throughout the period of the observations, from which all the stations occupied between 3°N and 3°S are selected. The vertical distribution of the east-west component of the current velocity at each of these stations is illustrated in Figs 26-47. The smooth curves in the figures are drawn for the convenience sake rather than for the interpolation or the smoothing, because such processes are less meaningful owing to various errors expected in the observed results, as will be discussed below.

The accuracy of these direct measurements is quite difficult to estimate, because in addition to the instrumental error of the current meter, some other errors are introduced. First, the measured value gives the average current velocity in a time interval of about 5 minutes, therefore it has a possibility of including some disturbances of shorter periods such as tidal currents which should be filtered out in the present discussions. Moreover, the time interval of the operation of a current meter is uncertain particularly in deeper layers, because one can not ascertain the time when a messenger strikes the current meter. The second error is due to the inavailability of the fixed reference in the open ocean. At some stations ship's drift is determined by reference to an island, otherwise by astronomical observation, whose accuracy can not be expected to be very high, and at the other stations the relative currents referred to the 800 meters or 600 meters levels are given. Hence this may introduce some errors in the zero-lines of the current speed in the figures, which can not be estimated at present. Thirdly, the depth of a current meter is determined by the wire angle at the surface and the wire length. Therefore, it also introduces a serious error in the depth of the observation more possibly in the deeper layers when the wire angle is large. This is the case near the

equator where the westward currents are often observed at the surface while the reversal currents are in the subsurface layer.

Under consideration of all errors described above, the results shown in Figs. 26–47 are interpreted as follows: Of six stations occupied between 130° and 140°E, one shows the westward current through all depths (Fig. 26), other two show the westward current in the upper 200 meters layer and no appreciable current in the lower layer (Figs. 27 and 28), and the other three the eastward current through all depths or below 200 meters (Figs. 29–31). Of two stations occupied between 140° and 150°E, one shows the westward current at the surface and the weak eastward current between the depth of 50 and 200 meters whose reality is, however, out side of the present accuracy (Fig. 32). The other shows the eastward current below the westward surface current at a depth of about 300 meters (Fig. 33). In the region between 150° and 160°E, eleven stations are occupied. One of them shows no appreciably definite current (Fig. 42), other two show the westward current through all depths (Figs. 40 and 43) and the other eight show the eastward current below the westward or weak surface current at a depth of about 200 meters (Figs. 34, 36–39, 41, and 44). All of the three stations occupied between 160° and 175°E show the eastward current below the weak westward surface current between the depth of 200 and 300 meters (Figs. 45–47).

Since the analysis made above on the basis of the geostrophic computation concerns with the average feature of the current, the results of the direct measurements should be interpreted in such a manner that gives some average state. Therefore, it may be concluded from the results of the direct measurements described above that an eastward current is frequently found at a depth of about 200 meters at and near the equator at least east of 150°E, although each measurement which gives the instantaneous feature shows considerable variety.

As the result of the present analysis made by two different ways, one based on the geostrophic computation and the other based on the direct measurements, an eastward subsurface current with its maximum velocity at the depth of about 200 meters is revealed at the equator in the Western Equatorial Pacific between 150° and 175°E. To the west of 150°E, it is weak or missing in the average state, and if it exists, it seems to be subjected to a considerable time variation. This result deduced here is also consistent

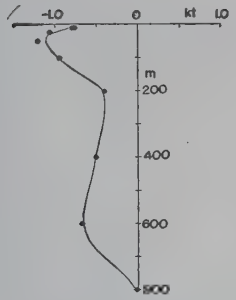

Fig. 26. Vertical profile of the east-west component (eastward positive) of the directly measured current velocity relative to 800 meters. *Kosyu*, Cruise 27, St. A20. 131°40.6′ E, 2°02.0′ N. May 23, 1933.

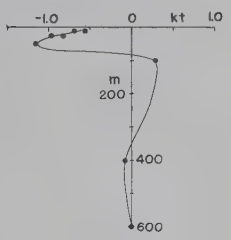

Fig. 27. Vertical profile of the east-west component (eastward positive) of the directly measured current velocity relative to 600 meters. *Kosyu*, Cruise 27, St. A21. 132°36.0′ E, 0°58.0′ N. May 24, 1933.

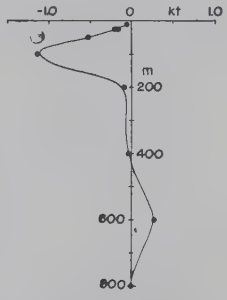

Fig. 28. Vertical profile of the east-west component (eastward positive) of the directly measured current velocity relative to 800 meters. *Kosyu*, Cruise 32, St. A56. 136°16.0′ E, 1°50.0′ N. July 3, 1934.

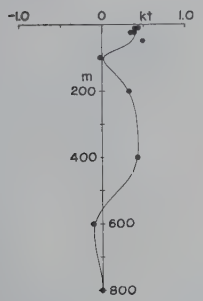

Fig. 29. Vertical profile of the east-west component (eastward positive) of the directly measured current velocity relative to 800 meters. *Kosyu*, Cruise 27, St. A25. 136°57.0′ E, 2°59.8′ N. May 27, 1933.

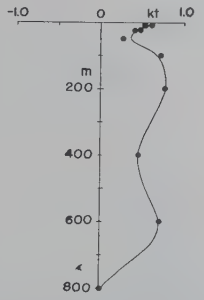

Fig. 30. Vertical profile of the east-west component (eastward positive) of the directly measured current velocity relative to 800 meters. *Kosyu*, Cruise 32, St. A53. 138°00.5′ E, 0°35.0′ N. July 4, 1934.

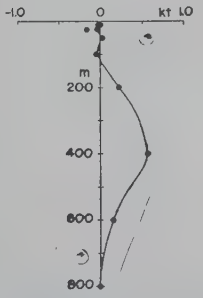

Fig. 31. Vertical profile of the east-west component (eastward positive) of the directly measured current velocity relative to 800 meters. *Kosyu*, Cruise 32, St. A51. 138°01.0′ E, 0°58.0′ N. July 5, 1934.

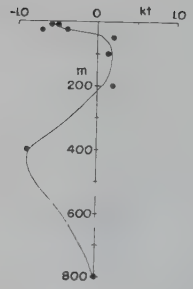

Fig. 32. Vertical profile of the east-west component (eastward positive) of the directly measured current velocity relative to 800 meters. *Kosyu*, Cruise 32, St. A29. 142°01.0′ E, 0°01.5′ N. July 17, 1934.

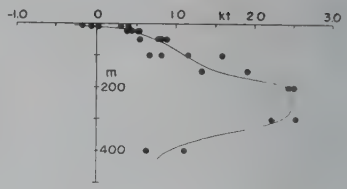

Fig. 34. Vertical profile of the east-west component (eastward positive) of the directly measured current velocity. Ship's drift is determined by the astronomical observation. *Mansyu*, St. 260. 154°22′ E, 0°02′ S. June 20, 1926.

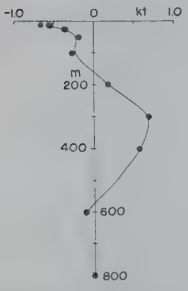

Fig. 33. Vertical profile of the east-west component (eastward positive) of the directly measured current velocity relative to 800 meters. *Kosyu*, Cruise 52, St. 59. 149°54.5′ E, 0°49.0′ S. June 14, 1938.

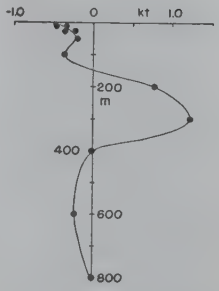

Fig. 35. Vertical profile of the east-west component (eastward positive) of the directly measured current velocity relative to 800 meters. *Kosyu*, Cruise 43, St. 67. 154°34.0′ E, 1°23.7′ N. Feb. 4, 1937.

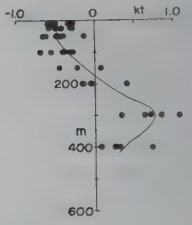

Fig. 36. Vertical profile of the east-west component (eastward positive) of the directly measured current velocity. Ship's drift is determined by the astronomical observation. *Mansyu*, St. 258. 154°49.5′ E, 2°25.5′ N. June 17, 1926.

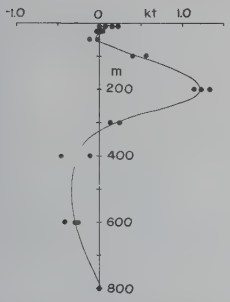

Fig. 37. Vertical profile of the east-west component (eastward positive) of the directly measured current velocity relative to 800 meters. *Kosyu*, Cruise 52, St. 64. 154°55.0′ E, 1°26.2′ N. June 20, 1938.

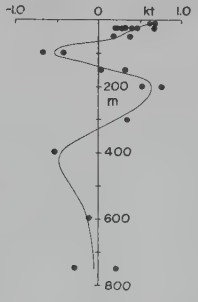

Fig. 38. Vertical profile of the east-west component (eastward positive) of the directly measured current velocity. Ship's drift is determined by reference to an island. *Mansyu*, St. 658. 154°57.0′ E, 1°08.0′N. Jan. 9, 1928.

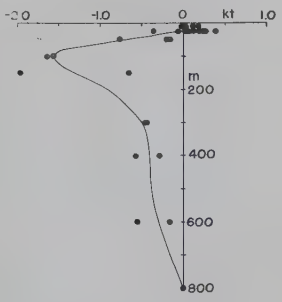

Fig. 40. Vertical profile of the east-west component (eastwad positive) of the directly measured current velocity relative to 800 meters. *Mansyu*, St. 657. 155°02.5′ E, 2°22.5′ N. Jan. 8, 1928.

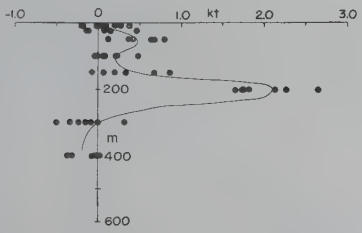

Fig. 39. Vertical profile of the east-west component (eastward positive) of the directly measured current velocity. Ship's drift is determined by reference to an island. *Mansyu*, St. 259. 155° 00.5′ E, 1°08.5′ N. June 18–19, 1926.

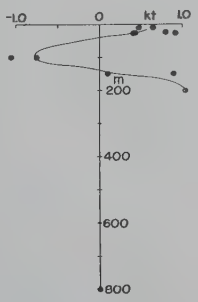

Fig. 41. Vertical profile of the east-west component (eastward positive) of the directly measured current velocity relative to 800 meters. *Mansyu*, St. 659. 155°03′ E, 0°12′ N. Jan. 10, 1928.

Fig. 42. Vertical profile of the east-west component (eastward positive) of the directly measured current velocity relative to 800 meters. *Kosyu*, Cruise 43, St. 65. 155°43.5′ E, 2°43.3′ N. Feb. 3, 1937.

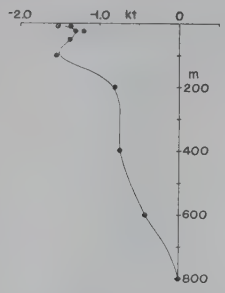

Fig. 43. Vertical profile of the east-west component (eastward positive) of the directly measured current velocity relative to 800 meters. *Kosyu*, Cruise 27, St. A46. 155°44.0′ E, 1°49.0′ S. Sept. 3, 1933.

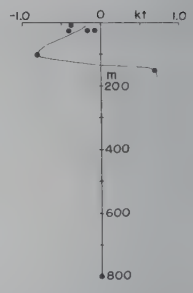

Fig. 44. Vertical profile of the east-west component (eastward positive) of the directly measured current velocity relative to 800 meters. *Mansyu*, St. 661. 157°19′ E, 1°16′ N. Jan. 11, 1928.

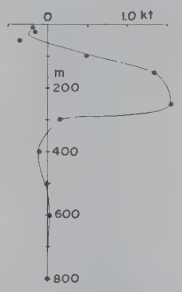

Fig. 45. Vertical profile of the east-west component (eastward positive) of the directly measured current velocity relative to 800 meters, *Kosyu*, Cruise 19, St. M10. 163°29.0′ E, 1°10.5′ N. May 24, 1932.

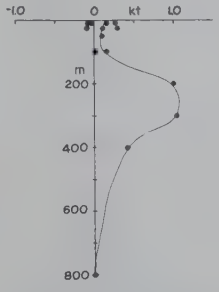

Fig. 46. Vertical profile of the east-west component (eastward positive) of the directly measured current velocity relative to 800 meters. *Kosyu*, Cruise 43, St. 43. 164°18.5′ E, 2°54.0′ N. Jan. 16, 1937.

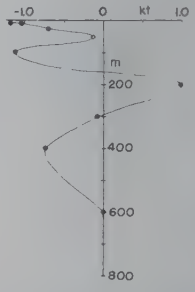

Fig. 47. Vertical profile of the east-west component (eastward positive) of the directly measured current velocity relative to 600 meters. *Kosyu*, Cruise 43, St. 36. 165°42.6′ E, 0°01.2′ S. Jan. 14, 1937.

with that of the recent current measurements in Jan.-Feb., 1958 reported by YOSHIDA *et al.* (1959).

5. *The South Equatorial Current and the equatorial upwelling*

The South Equatorial Current will be identified with the downward slope of the isobaric surfaces towards the equator from the southern boundary of the Equatorial Countercurrent. However, owing to the small gradient of the isobaric surfaces near the equator and small scale fluctuations of the isobaric surfaces which might be due to short period disturbances or might be observational errors, the quantitative estimation of the South Equatorial Current is very difficult so far as the goestrophic computations are concerned. Nevertheless, the dynamic sections and the surface dynamic topography referred to the 1000 db surface show, in most cases, the evidence of the South Equatorial Current to the south of the Equatorial Countercurrent throughout the equatorial region between 130° and 175°E. But there are several cases in which the South Equatorial Current disappears from the northern hemisphere and the Equatorial Countercurrent seems to extend to the southern hemisphere across the equator: In June, 1936, the dynamic topography in the region between 155° and 170°E reveals no maximum height in the northern hemisphere near the equator. This may indicate the extension of the Equatorial Countercurrent to the southern hemisphere across the equator. This is also the case in Oct., 1941 around 170°E, although the situation is less well defined than in June, 1936. As described in the preceeding section, the direct measurements of the

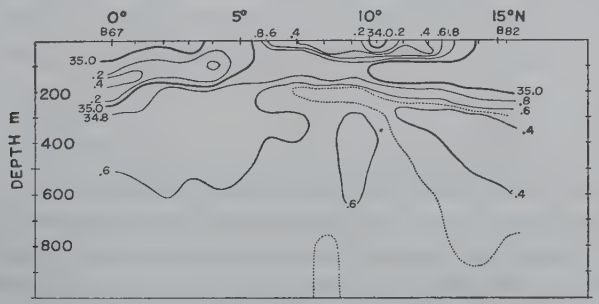

Fig. 48. Salinity section along 156°E. *Kosyu*, Cruise 32, Sts. B67-B82. Feb., 1935.

current in this region also show, at many stations, the westward or weak current at the surface, indicating the presence of the South Equatorial Current.

The southward extent of the South Equatorial Current and its behavior to the north of the New Guinea Island can not be clarified at all owing to the scarcity of the observations. A more detailed or quantitative description is beyond the present study, but it seems that the South Equatorial Current shows considerable time variations.

The upwelling at the equator is evident in the Eastern Pacific, but so far as the present analysis is concerned, no indication of the equatorial upwelling is found in the Western Pacific. Of course, in this analysis, no other data than temperature and salinity are available, and therefore the discussions are made on an insufficient basis.

As an indication of the equatorial upwelling, the vanishment of the salinity maximum layer at the equator, which extends from the southern hemisphere to the north at the depth of about 150–200 meters, is often pointed out (Cromwell, 1953, Austin, 1954). If this is really an indication of the equatorial upwelling, there is no upwelling, at least no intense upwelling at the equator of the Western Pacific, because in every salinity section prepared in this study, this salinity maximum tongue extends continuously from the southern hemisphere to the north across the equator without showing any interruption as illustrated in Fig. 48 by a typical example.

As the conclusion, at least, we can neither find the surface low temperature region due to the upward bend of the isotherms in the upper part of the thermocline layer near the equator nor the interruption of the high salinity tongue from the southern hemisphere, both of which are outstanding features in the Eastern Equatorial Pacific and are regarded as the evidence of the equatorial upwelling.

6. The dynamic section along the equator

It would be also of interest to describe about the longitudinal variation of the dynamic height of the isobaric surfaces along the equator. For this purpose, 51 stations which are occupied within a narrow equatorial zone between 30′N and 30′S are selected. The stations are unavoidably distributed more densely between 130° and 160 E than between 160 E and 180° as will be seen in the following table.

Table 4. Number of hydrographic stations along the equator.

Region	130°–140°E	140°–150°E	150°–160°E	160°–170°E	170°E–180°
Number of stations	11	12	18	6	4

The dynamic height anomaly of the surface referred to the 1000 db surface is plotted for each station indifferent to the seasons and the years (Fig. 49). The plotted points scatter very irregularly with a range of about 40

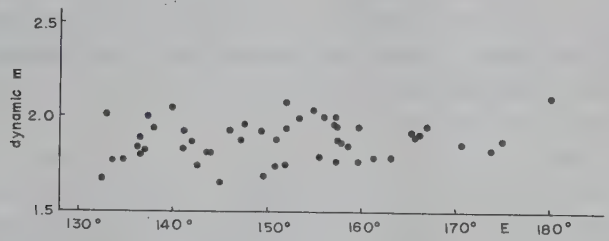

Fig. 49. Longitudinal variation of the surface dynamic height anomaly referred to the 1000 db surface along the equator.

dynamic centimeters and no definite slope is revealed throughout the region between 130°E and 180°. This range of 40 dynamic centimeters is nearly two thirds of the whole range of the longitudinal variation of the surface dynamic height along the equator between 130°E and 100°W obtained by Austin (1958).

If the stations are classified by seasons, the situation remains unaltered. Some other deeper isobaric surfaces also give the same result, but the range of the scatter is, of course, less than at the surface.

7. Summary and conclusions

Based on the oceanographic data in the Western Pacific during the period of 1925–1941, an oceanographic description of the Equatorial Current System is presented. Features of interest revealed by this analysis are:

(1) Although the Equatorial Countercurrent show considerable variations both in its location and transport, it exists between 3°N and 8°N on the average, and also it always exists except one case so far as the present data are concerned.

(2) In general the Equatorial Countercurrent seems to have its maximum velocity in the southern half of the current.

(3) Under the Equatorial Countercurrent, a westward current is often revealed between the depth of about 200 and 600 meters at about 5°–7°N.

(4) Sometimes, the Equatorial Countercurrent extends to the south across the equator at the surface.

(5) The Equatorial Countercurrent extends to the south in the subsurface layer, at least in the eastern region

(6) In the eastern region east of 150°E, an eastward subsurface current with its maximum speed at a depth of about 200 meters is revealed at and near the equator. This eastward current seems continuous with the Equatorial Countercurrent to the north of it.

(7) This eastward current at the equator is weak or missing to the west of 150°E.

(8) There is no clear indication of the equatorial upwelling in the Western Pacific.

(9) No definite slope of the isobaric surfaces is found along the equator between 130°E and 180°.

The present discussion of the current system essentially depends on the geostrophic computation. Hence, the uncertainty due to the somewhat arbitray choice of the reference level, due to some disturbances of small scale or short period, and due to some other errors introduced in the process of the dynamic computation is unavoidable. Moreover, in the surface layer, the stresses of the wind would modify the geostrophic current. The result of the analysis is interpreted under consideration of this uncertainty.

The eastward subsurface current at and near the equator revealed in this study is not a synoptic feature but an average, or climatological, one. Therefore further study of its synoptic feature is desirable. On the other hand, it also stimulates our interest whether or not this eastward current in the Western Pacific is continuous with the Equatorial Undercurrent of the Eastern Pacific. The answer to this question depends on future observations in the equatorial waters of the Central Pacific. In any case, however, it seems that somewhat different mechanisms maintain the eastward subsurface currents in the eastern and western parts of the Equatorial Pacific, because some differences are found between the features in the eastern and western parts. In

the eastern part, the indication of the equatorial upwelling, which is expected to play an important rôle in the dynamical mechanism of the *Cromwell Current* as discussed by YOSHIDA (1959) from the theoretical point of view, is evident, while such a distinct indication of the equatorial upwelling is not found in the west. And further, the eastward current in the west seems to be continuous with the Equatorial Countercurrent and also to show considerable time variations. These features different from those in the east might also suggest some differences of the mechanism of the maintenance.

In order to make clear these several points which are left for the future study, new systematic measurements of currents would be required. Our present effort, therefore, should be made in this direction.

Acknowledgements

The author wishes to express his hearty thanks to Dr. Koji HIDAKA of the Geophysical Institute, Tokyo University and to Dr. Masito NAKANO of the Meteorological College, Japan Meteorological Agency for their encouragements throughout the course of this study. The same thanks are due to Dr. Kozo YOSHIDA of the Geophysical Institute, Tokyo University for his stimulative discussions and suggestions and due to Dr. John A. KNAUSS of the Scripps Institution of Oceanography for his valuable suggestions, without them this study would be much less complete. The same thanks are also due to Messrs. Toshihiko TERAMOTO and Yutaka NAGATA for their critical discussions and to Mrs. Kazuko TSUCHIYA for her task of preparation of the manuscript and figures.

References

AUSTIN, T.S., (1954): Mid-Pacific oceanography, Part V. Transequatorial waters. May-June 1952, August 1952. *Special Scientific Report-Fisheries*, No. 136. 52 pp. U. S. Fish and Wildlife Service.

AUSTIN, T. S., E. D. STROUP, and M. O. RINKEL, (1956): Variations in the Equatorial Countercurrent in the Central Pacific. *Trans. Amer. Geophys. Union*, **37** (5), 558—564.

AUSTIN, T. S., (1958): Variations with depth of oceanographic properties along the equator in the Pacific. *Trans. Amer. Geophys. Union*, **36** (6), 1055—1063.

CROMWELL, T., (1953): Circulation in a meridional plane in the Central Equatorial Pacific. *J. Mar. Res.*, **12** (2), 196—213.

CROMWELL, T., R. B. MONTGOMERY, and E. D. STROUP, (1954): Equatorial Undercurrent in Pacific Ocean revealed by new methods. *Science*, **119** (3097), 648—649.

Hydrographic Department, Imperial Japanese Navy, (1933): The report of oceanic survey in western part of the North Pacific Ocean carried out by H. I. J. M. S. Mansyû from April to March 1928. *Bull. Hydrog. Dept.*, **6**, 1—458.

Hydrographic Office, Japan Maritime Safety Board, (1950—52): The results of oceanographic observations in the North-western Pacific Ocean. Nos. 3—5. *Hydrog. Bull.* Special Nos. 6, 8, 9.

KNAUSS, J. A. and R. PEPIN, (1959): Measurements of the Equatorial Countercurrent. *Nature*, **183**, 380.

KNAUSS, J. A., (1960): Measurements of the Cromwell Current. *Deep-Sea Res.*, **6** (4), 265—286.

—— (1961): The structure of the Pacific Equatorial Countercurrent. *J. Geopys, Res.*, **66** (1), 143—155.

REID, J. L., (1959): Evidence of a South Equatorial Countercurrent in the Pacific Ocean. *Nature*, **184**, Supplement No. 4, 209—210.

TSUCHIYA, M., (1955): On a simple method for estimating the current velocity at the equator, (II). *Rec. Oceanog. Works in Japan*, **2** (2), 1—6.

WYRTKI, K., (1957): Die Zirkulation an der Oberfläche der Südostasiatischen Gewässer. *Deutshe Hydrog. Zeit.*, **10** (1), 1—13.

YOSHIDA, K., (1959): A theory of the Cromwell Current (the Equatorial Undercurrent) and of the equatorial upwelling—An interpretation in a similarity to a coastal circulation ——. *J. Oceanog. Soc. Japan*, **15** (4), 159—170.

YOSHIDA, S., H. NITANI, and N. SUZUKI, (1959): Report of multiple ship survey in the equatorial region (I. G. Y.) Jan.-Feb., 1958. (in Japanese). *Hydrog. Bull.*, **59**, 1—30.

The Oceanographical Magazine
Vol. 13. No. 1, October 1961

Kuroshio in Enshū-nada (III)

—Variations of the depth of isotherms—

By

Shunji Konaga

Kobe Marine Observatory

(Received July 10, 1961)

Abstract: An internal wave of great amplitude may induce a considerably strong current and may change the oceanographic condition with its period.

We treat the interrelationship between the oceanographic condition and the variation of the depth of isotherms whose period is the same as the ordinary tide. Our conclusions are as follows: the induced surface current is of the order of 0.5 kt and internal wave propagates toward east in the cold water region.

1. Introduction

It has already been studied the behavior of the internal wave in the open ocean by many authors. But owing to the difficulties of the observations, that phenomenon has not yet been clarified sufficiently. Historically speaking, from the observation of Meteor Expedition the origin of the internal tide was discussed in the various ways by A. Defant (1950, 1952), considered two layered ocean and concluded that the resonance effect existed between the diurnal internal tide and inertial wave near the latitude of 30°. B. Haurwitz (1950) studied an influence of stationary current onto the internal wave. J. E. Fjoldstad (1936) resolved the partial differential equations by the numerical integration, and explained the vertical profile of internal wave. M. Yasui (1958) observed the internal wave in the region off Tohoku district of Japan, and pointed out that the diurnal and inertial wave were predominant. J. L. Reid (1956) observed internal wave in the region off California on board three vessels in 1950. His conclusion was that the internal wave was generated near the coast by ordinary tide and proceeded toward open ocean, deformed by the current. Other observations were carried out by P. Rudnick and J. D. Cochrane (1951),

W. MUNK (1945) and so on. W. KRAUSS (1957) resolved the linear partial differential equations in the two layered, horizontally infinite ocean, and defined the characteristic wave by means of the thickness of each layer and density difference in each layer, and concluded that it was resonated with astronomical tidal potential and calculated the variation of current by means of such an internal wave. M. RATTRAY (1957, 1960) treated the internal tide theoretically, assuming that its origin was near the coast, and he denied the resonance between it and inertial wave, and was led to the conclusion that the dissipation of energy was larger on the semidiurnal wave than on the diurnal wave. On the inertial internal wave, many author treated from the view point of the generation by wind and by travelling cyclone, *e.g.* T. ICHIYE (1955, 1958).

We consider the influences of internal wave upon the surface current system and short period variations of oceanographic conditions using the data of the observations in the cold water region off Enshū-nada in autumn, 1960.

2. *Oceanographic conditions in the region off Enshū-nada*

From October 21 to November 12, 1960, the oceanographic observations were carried out in the cold water region on board Shumpū Maru, Kobe Marine Observatory. The horizontal distribution of water temperature at 200 meters depth is depicted in figure 1, where the thick line indicates the cruise **A** which was carried out from October 28 to November 1, and the thin line, the cruise **B**, from November 5 to 9. And the vertical section across the Kuroshio along 137° 40'E longitude is in figure 2. At the glance of these figures we find that about 20 nautical miles the isotherm lines was displaced between the cruise **A** and **B**. This magnitude of variation was already pointed out by many authors, *e.g.* J. MASUZAWA (1958). The surface current also changed considerably large. The Kuroshio current velocities crossing the longitude 137° 40′ E is shown in the lower part of figure 2. It shows clearly that maximum value of current speed in the cruise **B** is nearly twice as large as in the cruise **A**. In figure 2 (b) we depict the vertical section on that meridian observed three times a day. The distribution of water temperature was not altered so large, but the surface current changed considerably large.

This phenomenon shows that the variation of shorter period, *i.e.* diurnal or semi-diurnal, has to be considered, and has already been observed on the north side of the Kuroshio by D. SHOJI *et al.*, Hydrographic Office, Japan. They

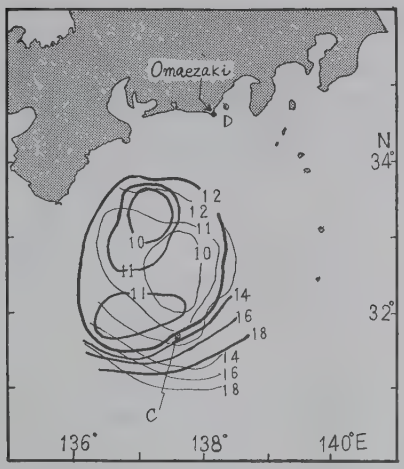

Fig. 1. The horizontal distribution of the water temperature at 200 meters depth in the region off Enshū-nada. The thick line shows in the cruise A and the thin line, in the cruise B.

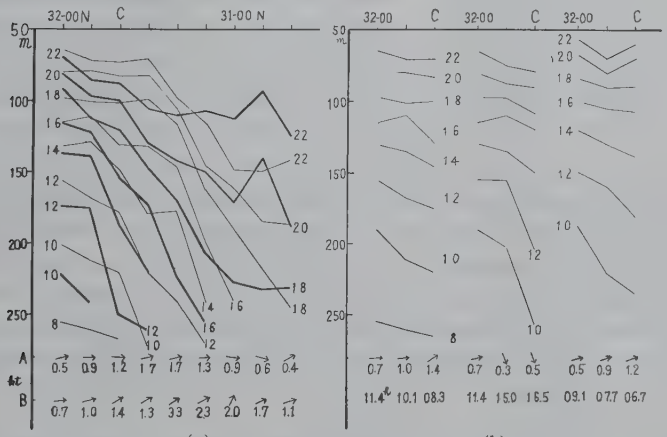

(a) (b)

Fig. 2.

(a): Vertical distribution of the water temperature along 137° 40′ E longitude, across the Kuroshio. The thick line shows in the cruise A and the thin line, in the cruise B. The arrows show the current velocity measured with GEK (in knots).

(b): Vertical distribution of the water temperature in the northern part of (a), which is observed three times a day.

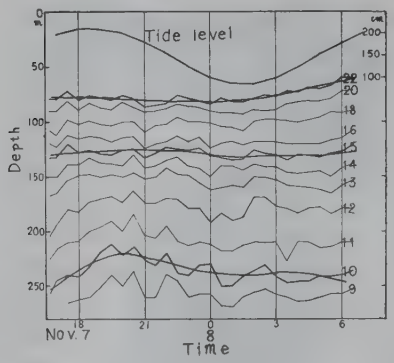

Fig. 3. Variations of the depth of isotherms at the station C and the tidal record at Omaezaki.

stated that the current varied with tidal period in 0.5 kt range. During the cruise **B**, at the station **C** (31° 40′ N, 137° 40′ E), which located at the northern edge of the Kuroshio, we measured the water temperature with BT every 30 minutes during about 14 hours. These results are depicted in figure 3 with tidal record at Omaezaki. This figure shows that the vertical displacement of isotherms at the fixed point **C** is considerably large. For example, the thermocline represented by 22°C isotherm is displaced about 20 meters and the isotherm of 10°C seems to move about 50 meters during only 14 hours. From the point of view of the horizontal displacement of current system, taking into account the horizontal gradient of the water temperature it is displaced about 30 nautical miles only in half a day. That large variation in such a short time interval may not be impossible but very difficult. Moreover, if we assume the horizontal displacement, the deeper the depth of isotherms becomes, the stronger the surface current must be, due to the warm Kuroshio current, but it is not so at this station. Hence we may owe the main part of its displacement to the vertical oscillation.

*3. Internal wave in Suruga Bay (Station **D**, 34° 42.7′ N, 138° 23.2′ E)*

It has been obviously explained that the internal tide exists in the bays or the coastal regions. We fortunately observed this phenomenon in Suruga Bay during 25 hours from September 21 to 22, 1960, by the fund of IAEA. These are depicted in figure 4 with tidal record at Omaezaki. These isotherms varied

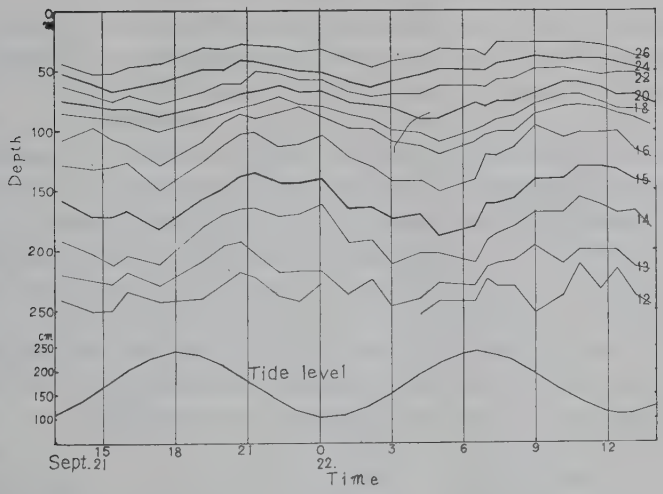

Fig. 4. Ditto at the station **D**.

with time is analysed harmonically, diurnal and semidiurnal wave. As the representatives 24°C, 20°C and 15°C are chosen. The amplitudes of the depth variations of these isotherms and the phase lag from the Omaezaki's tidal level are tabulated in table 1. By the same method the variation of the depth of isotherms (22°C, 15°C and 10°C) at the station **C** are analysed and also listed.

Table 1. The amplitude of the variation of the depth of isotherms, and the phase lag from the surface ordinary tide, at the station **C** and **D**.

In the Suruga Bay (Station **D**)	Amplitude		Phase lag (hours) refered to Omaezaki tide level		31-40N 137-40E (Station **C**)	Amplitude		Phase lag (hours) refered to Omaezaki tide level	
	diurnal	semi-diurnal	diurnal	semi-diurnal		diurnal	semi-diurnal	diurnal	semi-diurnal
Omaezaki tide level	cm 6.1	cm 63.9	0	0	Omaezaki tide level	cm 30.0	cm 45.7	0	0
24°C isotherms	m 4.6	m 10.5	+4.3	−2.0	22°C isotherms	m 10.8	m 3.4	+ 4.6	−0.4
20°C	2.3	12.2	−0.7	−3.1	15°C	0.5	2.8	+14.5	−0.9
15°C	4.1	21.9	+1.6	−3.2	10°C	44.6	17.9	+ 1.8	+2.1

It is obvious that the diurnal variations are predominant at the station C and the semidiurnal, at the station D. But the surface ordinary tide was more predominant in semidiurnal wave, because of the spring tide. M. YASUI showed that the diurnal and inertial wave were large but semidiurnal was small in the region off Tohoku district. The phase lag of internal wave from the surface ordinary tide happens to have almost same value at both stations in diurnal wave, but semidiurnal waves are some different in phase each other. We must consider the resonance with inertial wave, propagation and dissipation of energy and deformation of waves by the current system and the inhomogeneity of the density distribution, but these all are not so presicely defined that we may be able to treat these factors. From the only fact shown above, by which we are forced to accept the resemblance of the phenomena, however, we may not conclude that these two cases are originated in the same origin.

4. The surface current variation with internal wave

W. KRAUSS estimated the current induced from internal wave in a two layered, horizontally infinite ocean. It is reasonable to consider the horizontally infinite ocean, since the propagating velocity of the internal wave is very slow compared with the ordinary surface wave. The coordinate system is as follows; x axis is directed to the propagating direction of wave, and z axis is positive upward. The propagating internal wave is expressed as follows:

$$\eta = A\cos(\kappa x - \omega t)$$

where η is displacement of depth of isotherm from mean level, A is its amplitude, κ is its wave number and ω is the angular velocity. u, v and c are the velocity component of x, y direction and phase velocity of the wave respectively, which are shown as follows:

$$u = \frac{\omega}{\kappa h_1} \cdot \frac{h_2(\rho_1+\rho_2)}{\rho_1 h_2 + \rho_2 h_1} \cdot A\cos(\kappa x - \omega t),$$

$$v = \frac{f}{\kappa h_1} \cdot \frac{h_2(\rho_1+\rho_2)}{\rho_1 h_2 + \rho_2 h_1} \cdot A\sin(\kappa x - \omega t),$$

$$c = \sqrt{\frac{f^2}{\kappa^2} + \frac{\rho_2-\rho_1}{\rho_2} \cdot \frac{h_1 h_2}{h_1+h_2} \cdot g},$$

where ρ_1, h_1, are the density and thickness of upper layer and f is Coriolis factor. Suffix 2 shows of the lower layer. From the characteristic value of ω, the condition $\omega > f$ only have real solusion but we assume that the case $\omega \approx f$ is valid for upper formulae. So u and v are calculated numerically and combined.

The current ellipse is described. At the station C (31° 40′ N) the inertial period is about 23 hours, and this ellipse is almost perfect circle in the case of diurnal wave, but in semidiurnal wave it becomes an ellipse whose long axis is twice as short axis.

We depict the vertical distribution of the density at the station C in figure 5. It shows that the discontinuous layer exist about 70 meters depth. So we may consider that a discontinuous layer is represented by 22°C isotherm at the station C. Hence, $h_1=70$ m, $h_2=4000$ m, $\rho_1=1.023$, $\rho_2=1.025$ and $A=10.8$ m (diurnal), and 3.4 m (semidiurnal), respectively. We did not observe in what direction the internal wave propagated, but from the variation of the surface current measured with GEK and the phase of the internal wave—at 8 o'clock, the velocity of the current is ENE-1.4 kt, at 16 o'clock, SSE-0.5 kt and at 7 o'clock, ENE-1.2 kt, respectively, and at 8 o'clock and 10, the induced current are in maximum value toward the propagating direction of the internal wave, diurnal and semidiurnal, respectively—we assume that it propagates toward east. This assumption is consistent with that of J. L. Reid and M. Rattray, who considered that the internal wave is generated near the coast by the ordinary surface tide. From these we compute the induced current velocity and depict it in figure 6 by combining the diurnal and semidiurnal waves. Then we may know the actual current in any time at this station, provided that the ground current is known. We are surprised that the current induced by the internal wave is considerably large. This, however, is mean value in the upper layer. The vertical profile of the induced current may probably show the larger value near the discontinuous layer and smaller near the ordinary surface. From the observational fact we may not ascertain these results, except for the tendency of the variation of surface current. Next we consider the variation

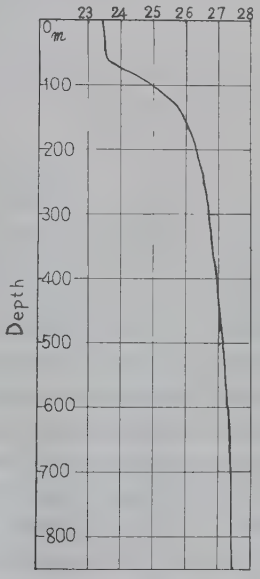

Fig. 5. Vertical distribution of the density in *situ* at the station C.

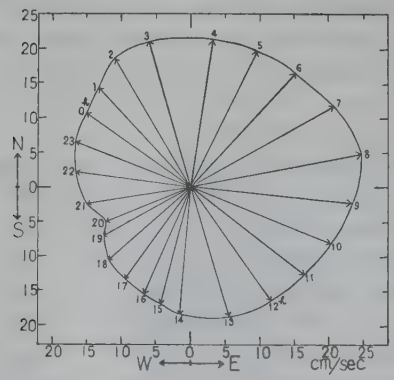

Fig. 6. The variation of the induced current. The numbers at the contour show time.

of the dynamic depth anomalies by the internal wave. A. DEFANT (1950 b) pointed out that an influence of internal waves complicated the dynamic topography. We calculate the dynamic depth anomalies above 200 meters depth, and find them to be varied in a range of about 5 dynamic centimeters. The mean temperature above 200 meters depth also changes in the range of 1°C. We must consider above fact and horizontal distribution of oceanographic elements becomes simpler by eliminating the effect of internal wave. The wave velocity is also calculated and it is about 1.2 m/sec., and the wave length is about 60 nautical miles which may be consistent with the diameter of the cold water region.

On shorter period internal wave we will treat in another paper, hence we state briefly here; several minutes to a few hours period waves exist but they have small amplitude or too short period to be observed in our method, since we can only carry out the observation at the ship's station which includes the error of a few nautical miles, and the measurement with BT is taken only in every 5 minutes,

5. Discussion

We consider that the internal wave originates in coastal region and propagates eastwards. But we may doubt that the diurnal wave is larger in the offshore region than in the coastal, and we may not clarify the resonance between

the inertial wave and diurnal internal tide. Moreover we do not know in what extent the horizontal displacement is in this period at the station C. In order to observe the internal wave more accurately, we need not only the longer period of observations, but also multiple ship survey, or we may not know the essential behavior of the internal wave. As the velocity is only a few percent of that of ordinary waves, which is of the same order of the ship's drift, the problem becomes more difficult to be resolved.

From KRAUSS' formula, y component of current, including Coriolis parameter, becomes much larger when the period of internal wave is very long and when we assume that his conditions of characteristic waves are neglected. If the wave velocity is constant, the wave number becomes smaller. Considering the wave of 14 days' period which is frequently observed in ordinary tide and of amplitude of 10 meters, y component of the induced current is about 250 cm/sec. It is too large to consider the variation of oceanographic condition in nature. Above speculations may allow us to consider whether this assumption is false or such waves do not exist. Internal wave of longer period, however, may be considered to exist due to the periodic wind stress, according to T. ICHIYE (1958) and K. YOSHIDA (1959). These waves are not observed in such simple observations and we may not detect them. From the analysis of surface tide, 4 day period was pointed out in the variation of tidal level in the equatorial regions by G. GROVES (1956). And the large scale variaton of the oceanographic condition might be produced by such a wave. The larger the depth of the thermocline is, the smaller the induced surface current is, if the amplitude of internal wave be constant. From the studies of the slick at the surface in the coastal region, when the wave height of the long internal wave is higher than a quarter of its mean depth, the slick or vortex may appear at the surface. From our observations at station C, the wave height of 22°C isotherm is about 20 meters and its mean depth is 75 meters. It satisfies the above condition, but we may have not seen such vortex or slick because of dark, although the surface current may change.

6. *Summary and conclusions*

(1) Predominant diurnal internal wave may exist in the cold water region off Enshū-nada, and induce the considerably large variation of surface current.

(2) From the phase of internal wave and actual variation, the internal wave proceeds eastward in the region.

(3) If we consider these variations of temperature from the point of view of the horizontal displacement in the current axis, we must expect that the displacement is about 30 nautical miles in half a day. It may not be impossible but very difficult. Even if it might be possible, we could not explain the relation of the variations between the current and the depth of isotherms.

(4) In the Kuroshio strong current we may not observe the internal wave in such a method as we have observed in the cold water region, since it is difficult to stay at a fixed position due to the ship drift, but we may suppose it may exist similar wave as in the cold water region, and the time variations of the current may be explained.

(5) One wave lengh of internal wave seems to be consistent with the diameter of the cold water region.

Acknowledgement: The author wishes to express his cordial thanks to Dr. K. HISHIDA and Dr. S. MORIYASU for their kind guidance and encouragement.

References

DEFANT. A. (1950): On the origin of internal tide waves in the open sea. *J. Mar. Res.*, **9.**
—— (1950): Reality and illusion in oceanographic surveys. *J. Mar. Res.*, **9.**
—— (1952): Über interne Wellen, besonders mit gezeiten Chracter. *D. Hydrogr. Zeits.*, JG 5. Heft 5, 6.
FJOLDSTAD. J. E. (1936): Interne Wellen. *Geophys. Publ.*, **10**(6).
GROVES. G. W. (1956): Periodic variation of sea level induced by equatorial waves in the easteries. *Deep. Sea Res.*, **3.**
HAURWITZ. B. (1950): The effect of ocean currents on internal waves. *J. Mar., Res.*, **9.**
ICHIYE. T. (1955): On the variation of oceanic circulation (V). *Geophys. Mag.*, **26**(4).
—— (1958): On long waves in a stratified, equatorial ocean caused by a travelling disturbance. *Deep Sea Res.*, **6.**
KRAUSS. W. (1957): Interne Wellen Grosser Amplitude (Teil 1). *D. Hydrogr. Zeits.*, JG. 10. Heft 5.
MASUZAWA. J. (1958): A short-Period fluctuation of the Kuroshio east of Cape Kinkazan. *Oceanogr. Mag.*, **10** (1).
MUNK. W. (1945): Internal waves in the Gulf of California. *J. Mar. Res.*, **4.**
RATTRAY. M. (1957): Propagation and dissipation of long internal waves. *Trans. Amer. Geophys.*, **38**(4).
—— (1960): On the coastal generation of internal tides. *Tellus*, **12**(1).
REID. J. L. (1956): Observation of internal tides in Oct. 1950. *Trans. Amer. Geophys.*, **37.**
RUDNICK. P. & J. P. COCHRANE (1951): Diurnal fluctuations in bathythermogarms. *J. Mar., Res.*, **10.**
YASUI. M. (1958): Internal waves in the open ocean. *Oceanogr. Mag.*, **10**(2).
YOSHIDA. K. (1960): The oceanic waves of days to months' periods. *Rec. Oceanogr. Works in Japan.*, **5**(2).

The Oceanographical Magazine
Vol. 13. No. 1, October 1961

Soundings of the Ramapo Deep*

By

Masashi YASUI, Jotaro MASUZAWA, Tsutomu SAWARA and Toshisuke NAKAI

Japan Meteorological Agency

(Received July 20, 1961)

1. *Introduction*

Since the great depth of 10,554 m in the southern part of the Japan Trench was discovered near 30° 40′ N, 142° 30′ E in 1933 from traverses of the U.S.S. Ramapo, this deep, called the Ramapo Deep, has been regarded as the deepest point in this trench. Although HESS and BUELL (1950) corrected this depth in consideration of the effect of the echo from the steep slope, still the depth remains to be 10,374 m. However, the great depth more than 10,000 m could not be found in the soundings near the Ramapo Deep on board both the R/V *S.F. Baird* (FISHER, 1957) and the R/V *Ryofu Maru* (NASU and others, 1960).

Precise soundings of the sea-floor topography near the Ramapo Deep were operated in 15 to 18 of June, 1960, as a part of the JEDS-3 (the Japanese Expedition of Deep Sea, the third cruise) program.

This paper is a summary for the results from this operation.

2. *Corrections on readings*

The R/V *Ryofu Maru* is equipped with the 811-type echo-sounder (MIYAJIMA, 1959) of Nippon Electric Co. Inc. The depth recorded by instrument can be read with the accuracy of ±5 m even at great depths. However, it seems quite difficult to determine the true depths from readings of these echograms, because of the following two reasons: (1) Sound velocity in sea water is not constant but different at different places and in different depths. (2) Puls-signals which are reflected from the nearest sea floor in the range of the beam of the transducer, namely side-echoes, are recorded on echograms.

* JEDS Contribution No. 24.

The mean sound velocity at a station can be obtained from the data of hydrographic cast. However, as a matter of fact, it is impossible to estimate vertical mean velocities at all positions of the ship underway. One of the authors (YASUI, 1957) presented the relationship between water temperature and densities and a trial method to estimate the dynamic depth anomaly at the sea surface referred to 1,000 m depth from the mean temperature in upper 400 m layer. As a rule, the sound velocity must mainly depend on the density of sea water. Therefore, it may be easily conceivable that the mean sound velocity might be estimated from BT-records.

In order to investigate this technique, we must empirically study the relationship between mean sound velocities from sea surface to bottom and mean temperature of upper 200 m layer. Difficulties of this study were mainly depend upon scanty of data of hydrographic casts in the water deeper than 1,000 m. Recently, hydrographical casts to the water deeper than 5,000 m have been done at several stations in the adjacent seas to Japan (MASUZAWA, 1961). From these data, we can obtain sound velocities in *situ*. Many tables computing sound velocities in *situ* have been presented by many authors. We computed sound velocities at all depths of all stations from these JEDS data by the aid of the OUTI's Table (OUTI, 1953). As a result of these computations, the local changes of sound velocities in the water deeper than 1,000 m are so slight that it seems quite reasonable to compute the average velocity from surface to bottom substituting these average sound distribution for the sound velocity in deeper layer than the deepest hydrographical cast in ordinary stations. Thus, we obtain scores of sets of relations between mean temperature in upper 200 m layers and vertical mean sound velocity in various water masses in the adjacent seas of Japan. These relationships are summarized in Figure 1. For practical purposes, the table, as shown in Table 1, was derived from the above-mentioned relationships. In the Japan Meteorological Agency, this table is used for corrections on readings of echograms.

The second problem, that is to say, slope corrections, is so knotty that we have not any complete method to settle in spite of efforts of many authors. Therefore, we are ordinarily obliged to read the shallowest mark of echogram when the bottom topography seems to be fairly simple, but if we recognize the complicated relief of sea floor, we used to estimate true depths by the method presented by SCHÜLER (1951).

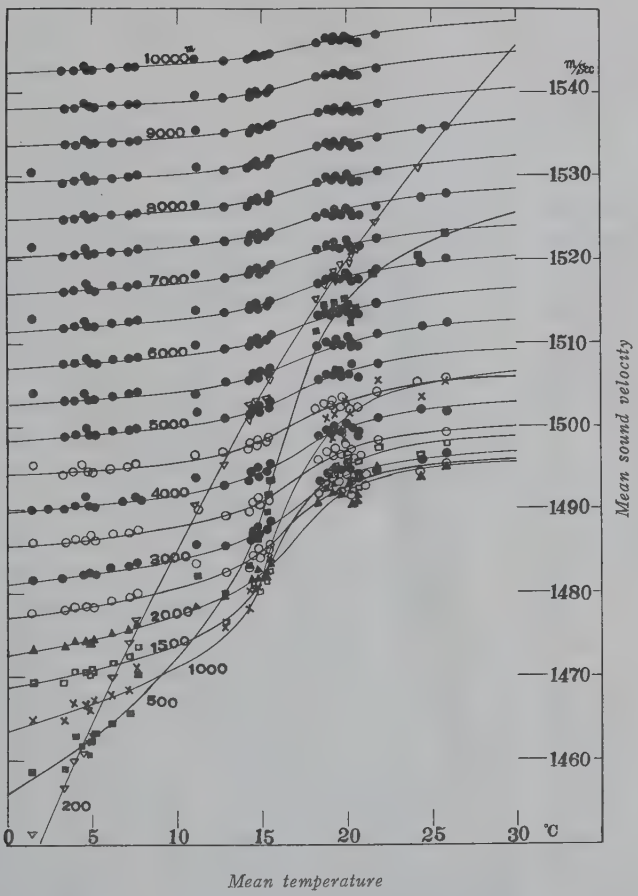

Fig. 1. Synthetic diagram shown relationship between mean temperature in upper 200 m layers and mean sound velocities in layers from surface to bottom.

3. *Results of soundings*

In programings, ten traverses each ten minutes of latitude were assigned covering the area of the Ramapo Deep from 29° 40′ N to 31° 10′ N, but the special traverse was added at the latitude of 30° 45′ N in order to ascertain the fine topography of the east flank of the trench. The echo-sounder was

Table 1. Correction for sound velocities (in meters).
$\overline{T}$; Mean temperatures in upper 200 m layers.
D; Readings on echograms.

D \ $\overline{T}$	0	2	4	6	8	10	12	14	16	18	20	22	24	26	28	30
200	−8	−7	−5	−4	−3	−2	−1	0	1	2	3	3	4	5	5	6
400	−12	−11	−10	−9	−8	−7	−5	−3	−1	2	4	5	6	7	7	8
600	−17	−16	−15	−14	−13	−11	−10	−7	−3	2	4	5	6	7	7	8
800	−21	−20	−19	−18	−17	−15	−14	−11	−5	0	2	4	5	5	6	6
1000	−24	−24	−23	−22	−20	−19	−18	−15	−8	−2	1	2	3	4	4	4
1200	−27	−26	−25	−24	−23	−22	−20	−17	−10	−5	−1	0	1	1	2	2
1400	−30	−29	−28	−27	−26	−25	−23	−20	−13	−7	−4	−2	−1	−1	0	0
1600	−32	−32	−31	−30	−28	−27	−25	−22	−16	−10	−6	−4	−3	−3	−2	−2
1800	−35	−34	−33	−32	−30	−29	−27	−24	−18	−12	−8	−6	−5	−5	−4	−4
2000	−37	−36	−35	−34	−32	−30	−28	−26	−21	−15	−11	−8	−7	−6	−6	−6
2200	−37	−36	−35	−34	−33	−31	−29	−26	−21	−15	−11	−9	−8	−7	−7	−6
2400	−38	−37	−36	−35	−34	−32	−30	−27	−22	−16	−12	−9	−8	−7	−7	−7
2600	−38	−37	−36	−35	−34	−32	−30	−27	−22	−16	−12	−10	−8	−8	−7	−7
2800	−38	−37	−36	−35	−34	−32	−30	−27	−22	−16	−12	−10	−8	−8	−7	−7
3000	−38	−37	−36	−35	−34	−32	−30	−27	−22	−16	−12	−10	−8	−7	−7	−6
3200	−36	−35	−34	−33	−32	−30	−28	−26	−21	−15	−10	−8	−6	−5	−4	−4
3400	−35	−34	−33	−32	−30	−29	−27	−24	−19	−13	−8	−5	−4	−3	−2	−2
3600	−33	−32	−31	−30	−28	−27	−25	−22	−17	−11	−6	−3	−1	0	1	1
3800	−30	−29	−28	−27	−26	−24	−22	−19	−15	−8	−3	0	1	3	4	4
4000	−27	−27	−26	−25	−24	−22	−20	−17	−12	−6	−1	2	4	6	7	8
4200	−24	−23	−22	−21	−20	−18	−16	−13	−8	−2	3	6	8	10	11	12
4400	−20	−19	−18	−17	−16	−15	−13	−9	−4	2	7	10	12	14	15	15
4600	−15	−15	−14	−13	−12	−11	−8	−5	0	6	11	15	17	19	19	20
4800	−10	−9	−9	−8	−7	−6	−3	0	5	12	17	20	22	24	15	25
5000	−5	−4	−4	−3	−2	0	2	5	10	17	22	25	27	29	30	31
5200	1	2	3	4	5	6	8	12	17	23	28	31	33	35	36	37
5400	7	8	9	10	11	12	14	18	23	29	33	37	40	41	42	43
5600	13	14	15	17	18	19	21	24	29	35	40	44	46	48	49	50
5800	21	22	23	24	25	27	29	32	37	43	48	51	54	56	57	58
6000	28	29	30	31	33	34	36	39	44	50	55	58	62	64	65	66
6200	37	38	39	40	41	43	45	48	53	59	64	68	70	72	73	74
6400	45	46	47	48	50	51	53	56	61	68	73	77	79	81	82	83
6600	54	55	56	57	59	60	62	65	71	77	82	86	88	90	91	92
6800	65	65	66	67	69	70	72	75	81	87	92	96	98	100	101	102
7000	75	75	76	77	78	80	82	85	90	96	101	105	107	109	111	112
7200	86	86	87	88	89	91	93	96	101	107	112	117	119	121	122	123
7400	97	97	98	99	100	102	104	107	112	119	124	128	131	133	134	135
7600	108	109	109	110	112	113	116	119	124	130	136	140	143	145	146	147
7800	120	121	122	123	124	126	128	131	136	142	147	151	154	157	158	160
8000	132	133	134	135	136	138	140	142	148	154	159	163	166	169	171	172
8200	145	146	147	148	149	151	153	156	162	167	173	177	180	183	185	186
8400	159	160	161	162	163	164	166	170	175	181	186	191	194	197	198	199
8600	173	174	175	176	177	178	180	184	189	195	200	205	208	211	212	213
8800	187	188	189	190	192	193	195	198	203	210	215	219	222	225	227	228
9000	201	202	203	204	206	208	210	212	218	224	229	233	236	239	241	242
9200	217	218	219	220	222	224	225	228	233	240	245	249	252	255	257	258
9400	232	233	234	236	237	239	241	243	249	255	261	265	269	271	273	274
9600	249	250	251	252	253	255	257	259	265	272	277	281	285	287	290	291
9800	266	267	268	269	270	272	274	276	282	288	293	298	301	303	305	307
10000	282	283	284	285	287	289	291	293	298	304	309	314	317	319	321	323

operated continuously and we could obtain records almost consistently. However, when strong gails blew, sea noises were too clamorous to distinguish echograms from noises. And, in a very few occasions, the echo was lost owing to the mishandling of apparatus. The records were read every six minutes, in which the ship travels about one neutical mile, and they were corrected by the method described in the previous section. The ship position was fixed every one hour by Loran, which has the accuracy of ±0.5 nautical miles in this area. The two values of the depth sounded independently at the point 30° 50′ N, 142° 36′ E where the ship track intersects were almost the same, so the accuracy of Loran as much as ±0.5 nautical miles seems quite reasonable.

The results of this sounding are summarized in Fig. 2 and 3. In these figures, the soundings were plotted at six minutes interval along the track, and continuous records were considered in drawing the contour.

Our bottom chart shows quite a good agreement with the soundings obtained by *S.F. Baird* (Fisher, 1957) with the exception of the neighbourhoods of 30° 40′ N, 142° 05′ E and 30° 30′ N, 142° 40′ E. In these areas the two configurations are almost coincident, when one obtained by the *S.F. Baird* are moved to the northeast as much as about three nautical miles.

This chart also shows rather a good agreement in general trend with the results reported by Nasu and others (1960), but we can not compare each other in details of the trench topography and amounts of the greatest true depth.

Figure 2 and 3 show some characteristic features of this trench. The bottom of the trench deeper than 9,000 m is generally not flat and there is a rise in the midst of the bottom of the trench. The most prominent example of this pattern is seen in the profile of the section **B**. The maximum depth on every profile occurs in the hollow west of this rise near the west flank.

The east flank of the trench bottom is generally steeper than the west flank. Especially, the east flank between 30° 35' N and 30° 48′ N is so steep that the records of echogram suddenly disappeared and in less than three minutes appeared again almost the same situation on the endless recorder as the depth which is about 1,000 m less than the previous depth (Fig. 4). Considering the ship speed, the steepness of this flank must be greater than 45°.

The deepest *Ryofu Maru* soudning of 9,704 m appears on the section **L** and the depth of 9,643 m appears on the section **B**. The maximum value of depths

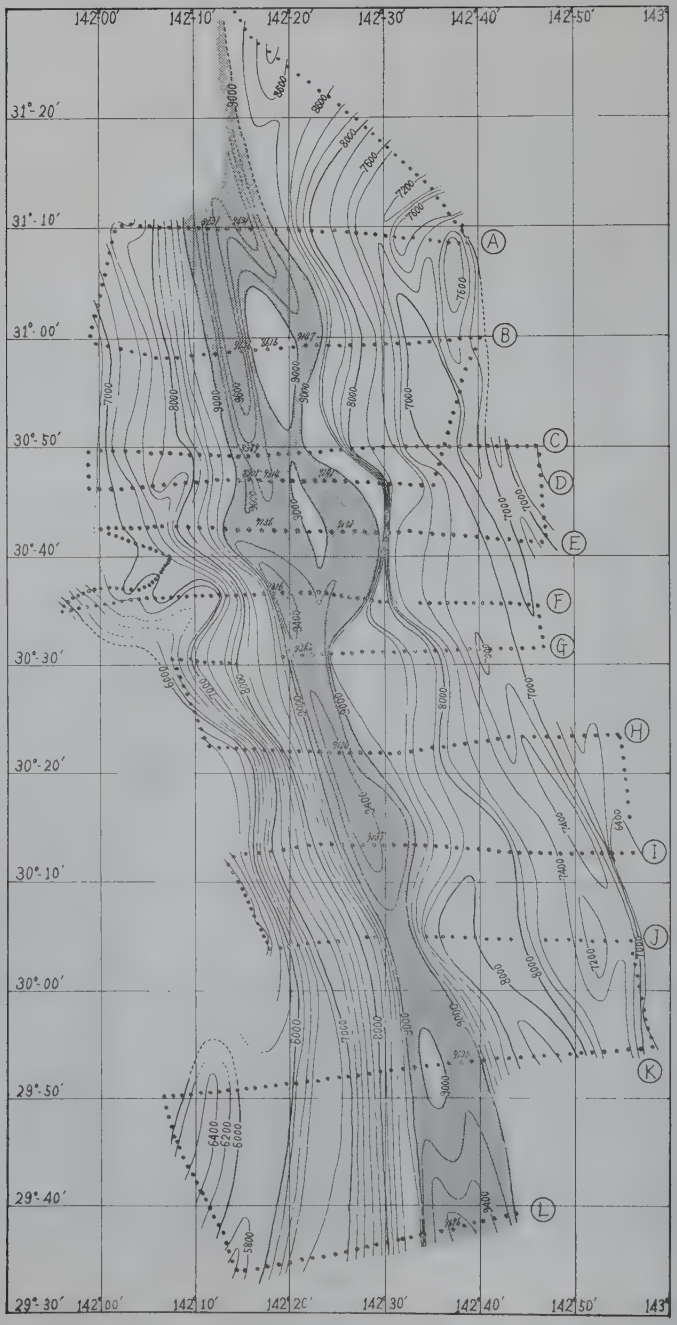

Topography of

Fig. 2. Sounding lines run by *Ryofu Maru*.

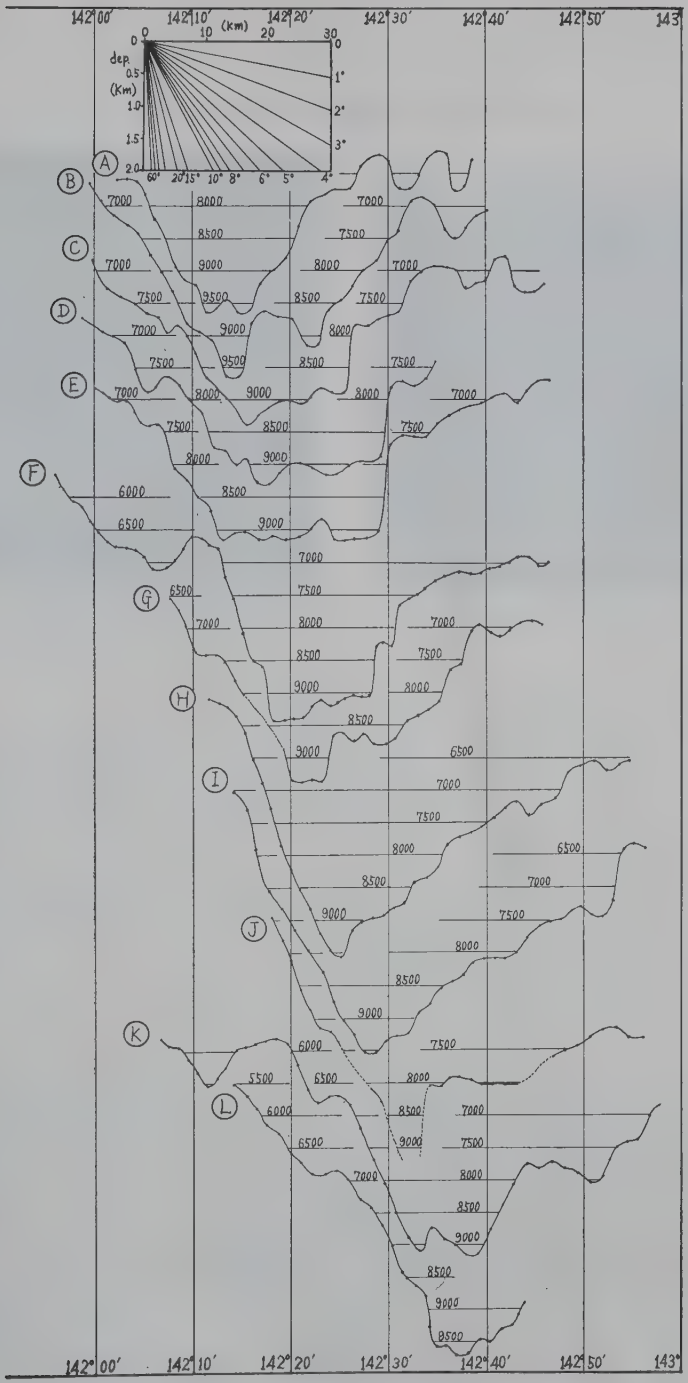

Ramapa Deep

Fig. 3. Bottom profiles with soundings plotted as depth.

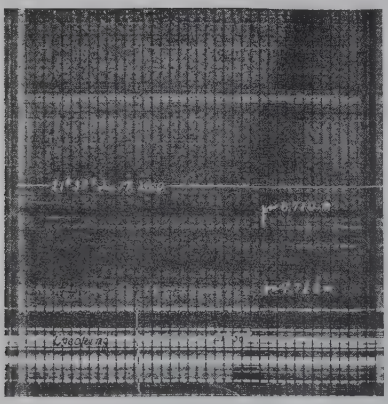

Fig. 4. Example of echograms at the steep east flank.

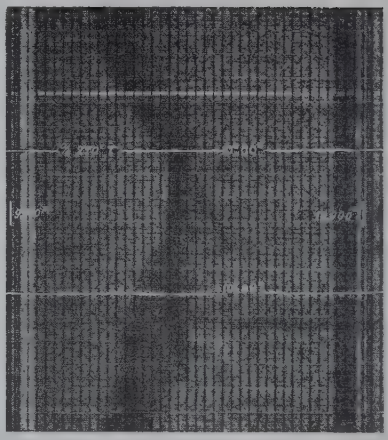

Fig. 5. Echograms at the deepest bottom along the Section L.

in the neighbourhood of the Ramapo is rather shallower.

In the deepest gorge, the echogram show fairly flat bottom (Fig. 5). The apparent width of the flat bottom is about 1,000 m on the echogram. However, the half diminish angle of our apparatus is 7.5° and the radius of the beam of pingings may be about 1,200 m in this depth, so the width of flat bottom may be more than 3,000 m.

Acknowledgement: The authors express their hearty thanks to the members of the Japanese Expedition of Deep Sea, the third cruise, for their kind co-operation for the soundings aboard the ship.

References

FISHER, R. L. (1957): On the soundings of trenches. *Deep-Sea Research*, **2** (1), 1957.

HESS, H.H. and N. W. BUELL, Jr. (1950): The greatest depth in the oceans. *Trans. Amer. Geophys. Un.*, **31** (3), 1950.

MASUZAWA, J. (1961): Preliminary reports of the Japanese Expedition of Deep Sea, the third cruise (JEDS-3). *Oceanogr. Mag.* **12** (2), 1961.

MIYAZIMA, T. (1959): Precision echo-sounder for oceanographical use (*in Japanese*). *Kokai*, No. 11 (Dec.), 1959. Nautical Society of Japan, Tokyo.

NASU, N., A. IIJIMA and H. KAGAMI (1960): Geological results in the Japanese Deep Sea Expedition in 1959. *Oceanogr. Mag.* **11** (2), 1960.

OUTI, M. (1953): Computation of the velocity of sound in sea water. *Bulletin of Kyoto Gakugei University*, Ser. B, No. 3, 60-68, 1953.

SCHÜLER, F. (1951): Die Abbildungstreue von Meeresboden-Profilen in Echogrammen. *Deutsche Hydrogr. Zeitschrift.* 4 (3), 1951.

YASUI, M. (1957): On the rapid estimation of the dynamic topography in the sea adjacent to Japan. *Rec. Oceanogr. Works in Japan*, 3 (1), 1957.

The Oceanographical Magazine
Vol. 13. No. 1, October 1961

Theoretical Investigations of Typhoon Surges along the Japanese Coast

By

Masamori Miyazaki — *Japan Meteorological Agency*
Takeo Ueno — *Japan Meteorological Agency*
Sanae Unoki — *Meteorological Research Inst.*

(Received July 31, 1961)

Contents

Chapter 1. Introduction
Chapter 2. Design of meteorological conditions
2.1 Typhoon models
2.2. Pressure distribution
2.3. Wind distribution
2.4. Track of designed typhoon
Chapter 3. Non-rotational cases
3.1. Basic equations
3.2. Making difference equations
3.3. Procedure of programing
3.4. Computations for Ise Bay
3.5. Computations for Tokyo Bay
Chapter 4. Rotational cases
4.1. Modifications for the non-rotational theory
4.2. Programing
4.3. Computations for Osaka Bay
4.4. Comparison with the observation
Chapter 5. Discussions and remarks

Abstracts: In this manuscript, we have computed the typhoon-surge distributions in Tokyo Bay, Osaka Bay, and Ise Bay by the numerical method. We are based on the hydrodynamic equations and integrate each equation numerically by giving the terms of external forces. The Ise Bay Typhoon in 1959, and some important others, are idealized and used as the typhoon models which induce these external forces. The effects of bottom friction and the Coriolis force are also taken into account. The computed results are thought to be in good agreement with the observed ones. However, we have now many underlying questions which still remain indeterminately.

Chapter 1. Introduction

Storm surges are abnormal deformations of sea-level induced by the atmospheric disturbances such as typhoons, hurricanes, or heavy extratropical

cyclones. Main causes of these surges are strong winds and atmospheric pressure anomalies accompanied with the disturbances. The water mass will be driven in the wind direction by tangential stresses exerting on horizontal layers, these stresses being transmitted from air to sea through the boundary surface. Anomalies of the atmospheric pressure will act to press or suck up the sea surface. Besides, in the coastal area, we have the considerable effects of the incoming water from the center of disturbance, coastal reflection, and the damping by bottom topographies.

Responses of these factors will be numercally estimated as the functions of known quantities or as the results of known dynamic processes, although we can hardly say that they are sufficiently made clear. The numerical computations of storm surges are now possible in this meaning, in which we solve the dynamic equations numerically by taking above factors into account.

Recently, computations are sped up extraordinarily by use of the electronic computers, and results can be obtained without avoidable assumptions or simplifications. We have now some investigations along this line. In 1954, Kivisild applied this method for the shallow-water surges with special exapmles for Lake Okeechobee. Hansen (1956) next computed the two-dimensional distributions of storm surges in North Sea induced by the Holland Storm in 1953. While, in U. S. A., Reid (1957) made the computations for surges in tidal estuaries, and Platzman (1958) for surges in Lake Michigan induced by the travelling squall line.

After the great damages of surges due to the Ise Bay Typhoon in 1959, we have also investigated similar problems by the numerical method (JMA 1960, JMA and Tokyo Metropol. Gov. 1960, JMA and 3rd Port and Harbor Const. Bureau 1961). In this manuscript, we intend to review procedures of our computations, discuss on their results, and point out underlying, indeterminable problems.

In the following chapter, we shall propose theoretical models of moving typhoon system, in which minute distributions of the surface atmospheric pressure and wind can be easily computed and are in agreement with observations at the neighboring meteorological stations. Next, in Chapter 3, we shall treat the non-rotational cases, where Coriolis terms are neglected and the bottom friction is assumed to be concerned with the current velocity linearly. The storm surges in Ise Bay and Tokyo Bay were computed under these assump-

tions. In Chapter 4, we shall further treat the rotational cases, where Coriolis terms are taken into account. The quadratic bottom-stress law is here modified and used by substracting the terms proportional to the surface stress. The storm surges in Osaka Bay were computed as an example of these cases. Lastly, in Chapser 5, we shall discuss on the results of computations, and on the indeterminable questions.

Chapter 2. Design of meteorological conditions

2.1. Typhoon models

Important bays along the Japanese Pacific Coast, such as Tokyo Bay, Osaka Bay, and Ise Bay, are often struck by heavy typhoon surges. In Table 2.1, we have listed some of the most disastrous surges in these bays.

Table 2.1. List of heavy storm surges in Tokyo Bay, Osaka Bay, and Ise Bay.

Bay		Typhoon		Track and Depth*			Maximum surge height (m)
Name	Opening to	Name	Date	Area	Direction	Depth mb	
Tokyo Bay	SSW	—	Oct. 1, 1917	50km NW of the Bay	NE	950	2.3
Osaka Bay	SW	Muroto	Sep. 21, 1934	West coast	NE	950	3.1
		Jane	Sep. 25, 1950	West coast	NNE	965	2.4
Ise Bay	SSE	Ise Bay	Sep. 26, 1959	50km west of the Bay	NNE	945	3.4

*) Data in the period of maximum surge

From Table 2.1, we easily found that these surges are caused by typhoons passing on the wastern side of bays. According to the statistics (Miyazaki 1957, etc.), it is also shown that surge heights are much higher in the case where the typhoon passes to the west of the bay opening to the southward than in the opposite case. Strong shoreward southerly winds in the dangerous semicircle often prevail in the former case, but both of the wind speed and direction are not so effective to heave the sea level in the latter case. In the following, we shall investigate on storm surges accompanied with above typhoons.

Now, one of the most important problems in studying storm surges is how to estimate the external forces induced by winds and pressure anomalies. In order to solve the dynamic equations of storm surges, we must be based on

the meteorological data in the actual typhoon field, from which the external forces can be computed numerically. In reality, however, meteorological data on the sea in the typhoon field can be hardly obtained in the present days, and we cannot help deducing them from ebservations on the land. In this meaning, we shalll design theoretical models of moving typhoon field from the observed data.

2.2. Pressure distribution

The pressure distribution in the typhoon field is usually represented as the function of the central distances. Some experimental formulas are now used, and, they are thought to be suitable for our purpose. One of the most simple formulas among them is that of Takahashi's (Takahashi 1939), which takes the following form

$$p=p_\infty-\frac{a}{1+r/r_0}, \tag{2.1}$$

where p_∞ is the pressure outside of the typhoon field, p the pressure at a distance r km from the center, a the pressure fall at the center, and r a constant distance in kilometers.

This formula is valid except for the close neighborhood of the typhoon center. Then, for instance, this formula may be used for the computations of Ise Bay surges. Typhoon passed about 50 km westward from the Bay, and we need no pressure values near the center.

However, this formula is not valid when the typhoon passes through or along the bay under consideration. In such a case, Fujita's formula (Fujita 1952)

$$p=p_\infty-\frac{a}{\sqrt{1+(r/r_0)^2}} \tag{2.2}$$

will be useful, where the notation is as mentioned above.

Fig. 2.1 shows the pressure-distance relations for the case of Ise Bay Typhoon. In this figure, the abscissa is the observed atmospheric pressure, and the ordinate is the distance from the typhoon center, respectively. The dotted curve in it represents the Takahashi's formula, and the solid curve represents the Fujita's formula. Parameters in these formulas p_∞, a, and r_0 are computed from cited observed values by the method of least squares. It is easily shown from this figure that Takahashi's formula gives too low pressure values near the center. However, except for the neighborhood of the

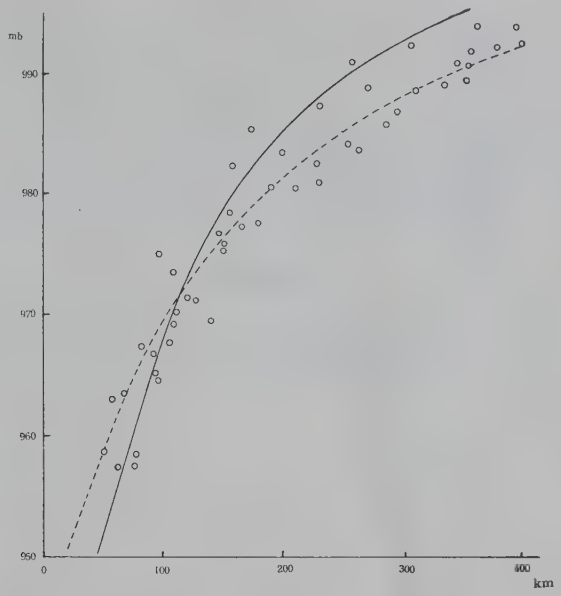

Fig. 2.1. The pressure-distance relations in the case of Ise Bay Typhoon, in which the solid curve represents the Fujita's formula and the dotted one the Takahashi's formula, respectively.

center, both formulas are considered to be agreeable with the observation. Similar relations are also shown for the cases of other typhoons.

Now, speaking more strictly, we have to consider time variations of these parameters. Among them, variations of parameters p_∞ and γ_0 are generally not so large, and they may be roughly supposed to be constant during the pass of typhoon near the area under consideration. But, the parameter a, which represents the depth of typhoon center, will be not always so. We shall use the medial values of a in the case of Tokyo Bay, but the filling up of the depth is considered in the case of Ise Bay, and the hourly values of a are given as the input data in the case of Osaka Bay.

2.3. Wind distribution

It is generally very difficult to determine theoretical forms of the wind distribution in a typhoon field.

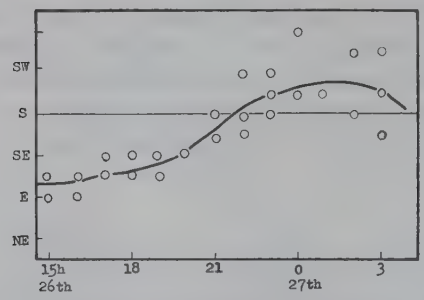

Fig. 2.2. Variations of the wind direction during the pass of the Ise Bay Typhoon.

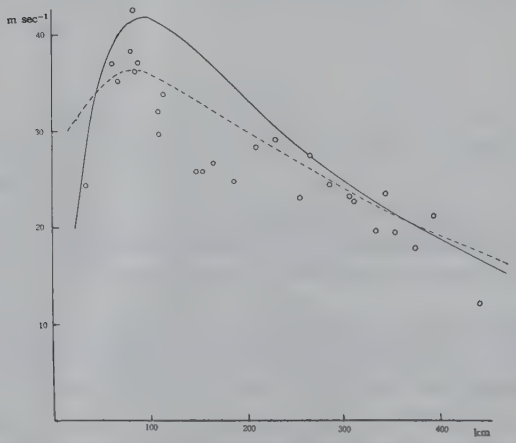

Fig. 2.3. Variations of the wind speed with the central distances in the case of the Ise Bay Typhoon, in which the solid curve represents the Fujita's formula and the dotted curve the Takahashi's.

At first, we consider that the wind speed is the function of the central distance, and the wind direction is that of the time, respectively. These assumptions are made for the case of Ise Bay Typhoon. Fig. 2.2 shows time variations of the observed wind direction, and Fig. 2.3 shows variations of the wind speed with the central distances. The computed values in Fig. 2.3 represent gradient winds corresponding to the pressure profile of Takahashi

(dotted curve), and Fujita (solid curve), respectively.

Except for Nagoya, observed wind speeds seem to be nearly comparable with computed curves, especially to that given by Takahashi's formula. Observed wind directions are also nearly equal to each other at the same instant. From these results, we may conclude that above rules hold approximately in this case. The Typhoon passed fairly westward of the Bay, and the area under consideration was all in her dangerous semicircle at that time.

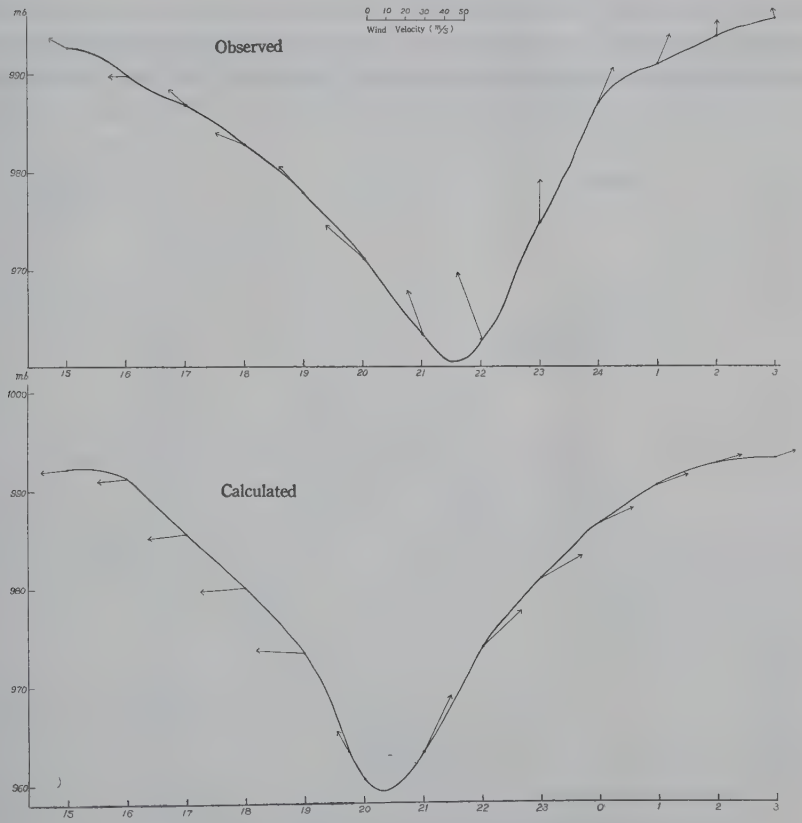

Fig. 2.4. The observed and computed variations of the wind and pressure at Nagoya during the pass of the Ise Bay Typhoon.

However, above rules will not hold wnen the typhoon passes through or along the bay, since the horizontal distribution of the wind direction will be no longer neglisible in such a case, and the wind speed will be fairly stronger in the dangerous semicircle than that in the navigable semicircle.

Thus, we further assume for general cases as follows.

(i) The wind system in the typhoon field consists of two parts. One is the symmetric wind system blowing around the typhoon center, and another is the field wind which drives the typhoon system.

(ii) The speed of the symmetric wind is proportional to that of the gradient wind Wg. The multiplier, or the proportional constant, is assumed to be equal to 0.7 when we make use the Takahashi's formula, and to 0.6 when we make use the Fujita's formula, respectively. The symmetric wind

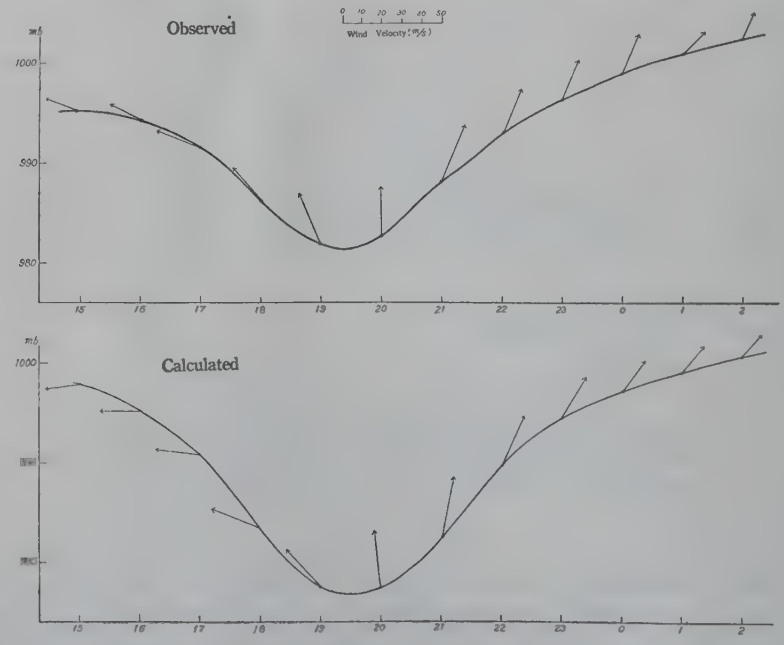

Fig. 2.5. The observed and computed variations of the wind and pressure at Yokohama during the pass of the Kitty Typhoon in 1949.

is also assumed to blow into the isobar with the angle 30°.

(iii) The field wind is proportional to the speed of the typhoon. Multiplier in this case is not constant, but varies with the scale of typhoon. It is generally large for typhoons of small scale, and small for typhoons of large scales. We further assume, for the time being, that the field wind speed decreases exponentially with the central distance. At a place 500 km distant from the center, the field wind is supposed to be $e^{-\pi}$ times the maximum value.

Fig. 2.4 and 2.5 indicate computed variations of the wind and the pressure at Nagoya during the pass of the Ise Bay Typhoon, and those at Yokohama during the pass of the Kitty Typhoon, respectively. The corresponding observed values are also shown in these figures. From these figures, we find

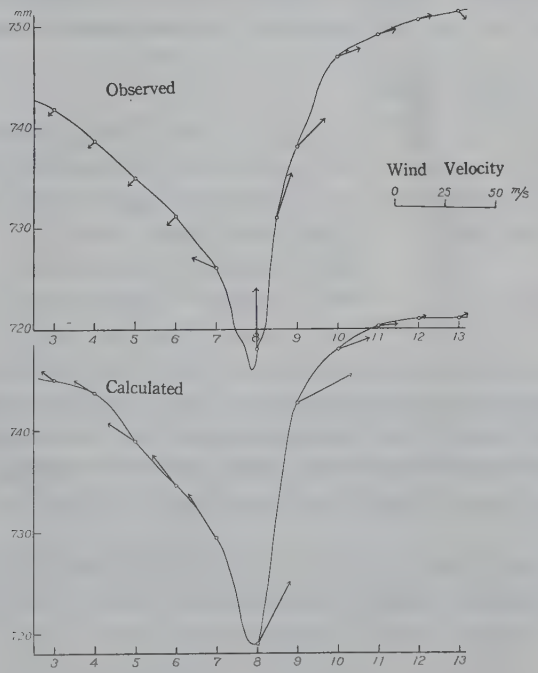

Fig. 2.6. The observed and computed variations of the wind and pressure at Osaka during the pass of the Muroto Typhoon in 1934.

that computed values are in fair agreement with the observed ones excepting somewhat discrepant occurrence of the minimum pressure in the case of Ise Bay Typhoon. To simplify the problem, we assumed the uniform movemt of the typhoon for these cases. Chief origins of anomalies are likely to be originated by this assumption.

Hourly locations of the typhoon center are read in as the observed data in the case of Osaka Bay. The agreement between computations and observations is bettered in this case (Fig. 2.6).

Now, we must notice that the above-mentioned rule of the wind distributions is not satisfactorily ascertained from the meteorological view-point in the present times. Especially, we have many questions for the assumption of the field wind, which will be closely related with the pattern of the upper layer wind. However, we have now only insufficient knowledge on this respect, and this rule may be modified by the development of investigations.

2.4. Track of designed typhoon

The computed typhoons are chosen from those passing to the westward of the bay under consideration. We choose the following typhoons from them.

(i)	for Ise Bay,	Ise Bay Typhoon (September, 1959) :
(ii)	for Tokyo Bay,	Typhoon on October 1 (1917),
		Kitty Typhoon (September, 1949) :
(iii)	for Osaka Bay,	Muroto Typhoon (September, 1934),
		Jane Typhoon (September, 1950).

Track of designed typhoons are primarily given from their hourly locations. At first (for cases of Ise Bay and Tokyo Bay), we suppose the typhoon moving with a constant velocity, and its track is adjusted to that of the actual one at two of these hourly locations before and after the nearest approach to the bay. We also assume the typhoons passing parallel to them for the purpose of comparison.

For the cases of Osaka Bay, we further assume more actual tracks which are adjusted to actual ones at hourly locations. In the intermediate hours, typhoons are supposed to move with the constant speed.

Chapter 3. Non-rotational cases

3.1. Basic equations

With enough approximation for the problem in the absence of Coriolis parameter, we have the following equations of motion and continuity,

$$\left.\begin{aligned}
&\frac{\partial u}{\partial t}=-g\frac{\partial}{\partial x}(\zeta-\zeta_0)+\nu\frac{\partial^2 u}{\partial z^2},\\
&\frac{\partial v}{\partial t}=-g\frac{\partial}{\partial y}(\zeta-\zeta_0)+\nu\frac{\partial^2 v}{\partial z^2},\\
&\int_{-\zeta}^{h}\left(\frac{\partial u}{\partial x}+\frac{\partial v}{\partial y}\right)dz=-(w)_{z=h}+(w)_{z=h},
\end{aligned}\right\} \tag{3.1}$$

where x, y, and z denote the cordinates of a rectangular system, and they are chosen eastward, northward, and downward from the origin on the mean sea surface, respectively. t is time, u, v, and w are the x, y, and z components of the current velocity, respectively, ζ is the surface elevation, ζ_o is the statical elevation corresponding to the pressur fall, g is the acceleration of gravity, h is the mean water depth, and v is the vertical eddy viscosity.

The surface and bottom conditions are

$$\left.\begin{aligned}
&\nu\frac{\partial u}{\partial z}=-\tau_s^{(x)},\quad \nu\frac{\partial v}{\partial z}=-\tau_s^{(y)},\\
&w=-\frac{d\zeta}{dt}=-\frac{\partial\zeta}{\partial t}-u\frac{\partial\zeta}{\partial x}-v\frac{\partial\zeta}{\partial y},
\end{aligned}\right\}\ \text{at the surface,}$$

and (3.2)

$$\left.\begin{aligned}
&\nu\frac{\partial u}{\partial z}=-\tau_b^{(x)},\quad \nu\frac{\partial v}{\partial z}=-\tau_b^{(y)},\\
&w=\frac{dh}{dt}=u\frac{\partial h}{\partial x}+v\frac{\partial h}{\partial y},
\end{aligned}\right\}\ \text{at the bottom,}$$

respectively; where τ_s and τ_b are the surface and bottom stress, and the suffixes (x), (y) mean their x and y components, respectively.

Now, if we use the components of the volume transport vector s_x, s_y defined by

$$s_x=\int_{-\zeta}^{h}u\,dz \quad\text{and}\quad s_y=\int_{-\zeta}^{h}v\,dz, \tag{3.3}$$

instead of u and v, the above equations will become

$$\left.\begin{aligned}
&\frac{\partial s_x}{\partial t}=-g(h+\zeta)\frac{\partial}{\partial x}(\zeta-\zeta_0)+\tau_s^{(x)}-\tau_b^{(x)},\\
&\frac{\partial s_y}{\partial t}=-g(h+\zeta)\frac{\partial}{\partial y}(\zeta-\zeta_0)+\tau_s^{(y)}-\tau_b^{(y)},\\
&\frac{\partial\zeta}{\partial t}=-\frac{\partial s_x}{\partial x}-\frac{\partial s_y}{\partial y}.
\end{aligned}\right\} \tag{3.4}$$

In (3.4), the ζ terms in the form $(h+\zeta)$ are originally of the same order to the inertia terms which are here neglected. However, in our cases, ζ terms are often more important than linear terms for shallow waters as long as ζ is comparable or larger than h. In contrast with them, inertia terms are at most comparable to the linear terms. For instance, ζ often exceeds 3 m near the bottom of Tokyo Bay when a powerful typhoon approaches, while the mean depths h are less than this value at many mesh points in this area. In these cases, ζ terms in the form $(h+\zeta)$ are undoubtfully more important than the corresponding h terms. In cntrast with it, the current speeds and their differences between the neighboring mesh points are at most 1 m/s or so in this area, and they are within fractions of above terms. For all these facts, the inertia terms are generally not of the primary importance, and we can neglect them in the first approximation.

Next, it will be our important problem how to express the stress terms τ_s and τ_b by the known quantities. So far as the most reasonable expression for the surface stress τ_s, we have

$$\tau_s=\gamma^2\rho_a W^2, \tag{3.5}$$

where ρ_a is the atmospheric density, W the velocity of wind at the anemometer height, and γ^2 a constant. According to MUNK and others, we have $\gamma^2=0.0026$ (c. g. s.) for the wind speed from about 6 m/s to 20 m/s.

The formula (3.5) was obtained in the neutral and stable states of the lower atmosphere, and not sufficiently examined in other states. Recent studies also report that γ^2 lies between 0.001 and 0.003 for the wind speeds above-mentioned, and their mean value is fairly less than 0.0026, while in some papers it is asserted that this value increases with the wind speed. So it will be very difficult to answer the question if we can use the relation (3.5) for very strong winds such as 40 m/s. It is only because we have now no generally admitted relations between the wind and the surface stress that we are obliged to apply the value 0.0026 given by MUNK and others in this computation.

We have also few studies on the form of bottom stress, which are considered to be reliable. HANSEN and others (loc. cit.) provided from the similarity to the case of the surface stress that

$$\tau_b=\eta\rho_w|\boldsymbol{V}|\boldsymbol{V}, \tag{3.6}$$

and adopted for η the same value 0.0026 as γ^2, where $\mathbf{V}$ denotes the mean velocity vector of currents. It is said that (3.6) holds for tidal currents, but

it is still doubtful if it holds in cases of storm surges where we have strong current gradients from surface to bottom.

Reid (1957) recently modified (3.6) as follows,

$$\tau_b=\gamma_b{}^2\rho_w|V|V-5\gamma_b\tau_s, \tag{3.7}$$

where he assumed that the tangential stress τ is in proportion to the depth. Yamada (1950) also obtained the the relation

$$\tau_b=\frac{3\nu\rho_w}{h}V-\frac{\tau_s}{2}, \tag{3.8}$$

where he provided that the current velocity is zero at the bottom, and that it is represented by a quadratic formula with respect to the depth. Now, if ν is independent of V, τ_b is proportional to V. On the other hand, if we provide that ν is proportional to V, then (3.8) will become similar to (3.7) except constants. In reality, we only know about ν that its value increases with the scale of the turbulence, which is concerned with the current velocity and the water depth.

For the cases of Ise Bay, we first assumed in (3.8) that ν is independent of the depth or current. However, we later assumed it to be proportional to the depth, and put

$$\nu=\nu'(h+\zeta) \tag{3.9}$$

Of course, we can hardly think that the stress variation is simply represented by the linear law, or that the quadratic formula indicates the sufficient distribution of the current with respect to the depth. We are going to study on this problem in later papers.

On boundary conditions, we take

$$s_x=s_y=0 \tag{3.10}$$

on the shoreline, while all the volume-transport vectors will be not disappear along the artificial sea shore such as the breakwater. In our study, except for the computations of dike effects on storm surges, the assumtion of the natural slope would not make big errors along the coastal line.

The last problem is the conditions at the mouth of the bay. Provided that the water is deep enough outside of the bay mouth, the surge height at the mouth will equal to ζ_o, the statical elevation corresponding to the pressare fall. Recent studies reported that, owing to both the large-scale edge waves and seiches caused by the meteorological disturbances approaching to the continental shelf, the elevations at the mouth are much higher than those estimated from the pressure fall. The direct long waves travelling from the typhoon center

will be also enlarged in shallow waters. However, we have not enough knowledge to represent it quantitatively so far. We thus extend the boundary as offshore as possible, where we put

$$\zeta=\zeta_0. \tag{3.11}$$

Now, it is our question how to solve the equations (3.4) under the conditions (3.5), (3.8) (or (3.7)), (3.10), and (3.11) by the numerical method, and they will be expressed in the following paragraphs.

3.2. *Making difference equations*

In order to solve the dynamic equations numerically, we must rewrite them by difference equations. We have now many methods of making differences, such as the progressive, regressive, and central differences, and the combinations of them. We here adopted the central differences from them after HANSEN and PATZMAN, which give more precise results than the progressive or regressive ones by the same mesh intervals.

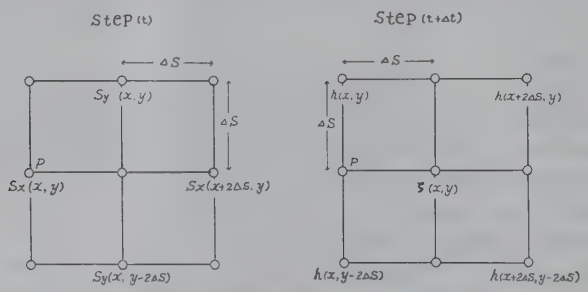

Fig. 3.1. Arrangement of mesh points.

If we compute the numerical values of variables at the mesh points shown in Fig. 3. 1, and at the time intervals of $2\Delta t$, the first equation of (3.4) will become

$$\{s_x(x,y,t+2\Delta t)-s_x(x,y,t)\}/2\Delta t=-g\{h(x,y)+\zeta(x,y,t+\Delta t)\}\times$$
$$\times\{\zeta(x,y,t+\Delta t)-\zeta(x-2\Delta x,y,t+\Delta t)-\zeta_0(x,y,t+\Delta t)+\zeta_0(x-2\Delta x,y,t+\Delta t)\}/$$
$$/2\Delta x+\tau_s^{(x)}-\left[\frac{3\nu}{\{h(x,y)+\zeta(x,y,t+\Delta t)\}^2}\cdot\frac{s_x(x,y,t+2\Delta t)+s_x(x,y,t)}{2}-\right.$$
$$\left.-\frac{\tau_s^{(x)}}{2}\right]. \tag{3.12}$$

Similary, we have from the second and third equations

$$\left.\begin{aligned}
&\{s_y(x,y,t+2\Delta t)-s_y(x,y,t)\}/2\Delta t=-g\{h(x,y)+\zeta(x,y,t+\Delta t)\}\times\\
&\quad\times\{\zeta(x,y+2\Delta y,t+\Delta t)-\zeta(x,y,t+\Delta t)-\zeta_0(x,\ y+2\Delta y,\ t+\Delta t)+\\
&\quad+\zeta_0(x,y,t+\Delta t)\}/2\Delta y+\tau_s^{(y)}-\Big[\frac{3\nu}{\{h(x,y)+\zeta(x,y,t+\Delta t)\}^2}\cdot\\
&\quad\cdot\frac{s_y(x,y,t+2\Delta t)+s_y(x,y,t)}{2}-\frac{\tau_s^{(y)}}{2}\Big],\\
&\{\zeta(x,y,t+3\Delta t)-\zeta(x,y,t+\Delta t)\}/2\Delta t=-\{s_x(x+2\Delta x,y,t+2\Delta t)-\\
&\quad-s_x(x,y,t+2\Delta t)\}/2\Delta x-\{s_y(x,y,t+2\Delta t)-\\
&\quad-s_y(x,y-2\Delta y,t+2\Delta t)\}/2\Delta y.
\end{aligned}\right\}\qquad(3.12')$$

Now, taking $\Delta x=\Delta y=\Delta s$, and introducing new variables s_x', s_y' given by

$$\left.\begin{aligned}
s_x'&=s_x\cdot\frac{\Delta t}{\Delta s},\\
s_y'&=s_y\cdot\frac{\Delta t}{\Delta s},
\end{aligned}\right\}\qquad(3.13)$$

(3.12) and (3.12') are simplified as follows.

$$\left.\begin{aligned}
&s_x'(x,y,t+2\Delta t)=a(x,y)s_x'(x,y,t)-b(x,y)\times\\
&\quad\{\zeta(x,y,t+\Delta t)-\zeta(x-2\Delta s,y,t+\Delta t)-\zeta_0(x,y,t+\Delta t)+\\
&\quad+\zeta_0(x-2\Delta s,y,t+\Delta t)\}+c(x,y)\tau_s^{(x)},\\
&s_y'(x,y,t+2\Delta t)=a(x,y)s_y'(x,y,t)-b(x,y)\times\\
&\quad\{\zeta(x,y+2\Delta s,t+\Delta t)-\zeta(x,y,t+\Delta t)-\zeta_0(x,y+2\Delta s,t+\Delta t)+\\
&\quad+\zeta_0(x,y,t+\Delta t)\}+c(x,y)\cdot\tau_s^{(y)},\\
&\zeta(x,y,t+3\Delta t)=\zeta(x,y,t+\Delta t)-s_x'(x+2\Delta s,y,t+2\Delta t)+\\
&\quad+s_x'(x,y,t+2\Delta t)-s_y'(x,y,t+2\Delta t)+s_y'(x,y-2\Delta s,t+2\Delta t),
\end{aligned}\right\}\qquad(3.14)$$

where

$$\left.\begin{aligned}
a(x,y)&=\Big[1-\frac{3\nu\Delta t}{\{h(x,y)+\zeta(x,y)\}^2}\Big]\Big/\Big[1+\frac{3\nu\Delta t}{\{h(x,y)+\zeta(x,y)\}^2}\Big],\\
b(x,y)&=g\{h(x,y)+\zeta(x,y)\}\Big(\frac{\Delta t}{\Delta s}\Big)^2\Big/\Big[1+\frac{3\nu\Delta t}{\{h(x,y)+\zeta(x,y)\}^2}\Big],\\
c(x,y)&=\frac{3(\Delta t)^2}{\Delta s}\Big/\Big[1+\frac{3\nu\Delta t}{\{h(x,y)+\zeta(x,y)\}^2}\Big].
\end{aligned}\right\}\qquad(3.15)$$

Provided that ν is proportional to the water depth, the terms

$$\frac{3\nu\Delta t}{\{h(x,y)+\zeta(x,y)\}^2}$$

in (3.15) will be rewritten as

$$\frac{3\nu'\Delta t}{\{h(x,y)+\zeta(x,y)\}}.$$

The variables $a(x,y)$, $b(x,y)$, and $c(x,y)$ are generally the functions of

time as long as ζ terms in (3.15) are not negligible, and they are computed at every 20 minutes in our investigation, where we take

$$\zeta(x, y)=\frac{1}{3}\{\zeta(x, y)+\zeta(x-2\Delta s, y)+\zeta(x, y+2\Delta s)\}. \tag{3.16}$$

However, they will be constant when ζ terms in (3.15) are negligible, and they are computed before the step by step computations in this case.

In (3.14), the first two equations represent the computations at the time step $t+\Delta t$, where $t=t_o$ (epoch) $t_o+2\Delta t$, $t_o+4\Delta t$, ……. The third equation represents the computations at the time step $t+2\Delta t$, where t changes as mentioned above. The numerical values at the epoch will be given from the initial conditions, which are

$$\begin{aligned} &\text{at } t=t_0, && S_x'=S_y'=0 && \\ &\text{at } t=t_0+\Delta t, && \zeta=\zeta_0 && \text{(at the mouth), and} \\ & && =0 && \text{(except for the mouth).} \end{aligned} \tag{3.17}$$

Thus, we have the distributions of S_x' and S_y' for the time steps $t=t_o$, $t_o+2\Delta t$,, $t_o+4\Delta t$, ……, and ζ for the time steps $t=t_o+\Delta t$, $t_o+3\Delta t$, $t_o+5\Delta t$, ……, respectively.

Now, it will be well-known that the condition

$$\frac{\Delta s}{\Delta t}>\sqrt{2gh_{\max}} \tag{3.18}$$

must hold in order to carry out stable computations, where h_{max} denotes the maximum depth at mesh points. Strictly speaking, the condition (3.18) will be somewhat modified under the existence of frictional terms. The right-hand term in (3.18) will be then rewritten by

$$\sqrt{2g\left|(h+\zeta)\middle/\left\{1+\frac{3\nu\Delta t}{(h+\zeta)^2}\right\}\right|_{\max}}. \tag{3.18'}$$

However, (3.18′) will be simplified as (3.18) in sufficient approximation as long as h_{max} is more than dozens of meters.

We have chosen in the case of Ise By $\Delta s=2$ (km), $h_{max}=60$ (m), and $\Delta t=54.5$ (sec), and in the case of Tokyo Bay $\Delta s=1.5$ (km), $h_{max}=66$ (m), and $\Delta t=35.3$ (sec), respectively.

The numerical computations can be actually carried out by the above-mentioned method. However, unavoidable errors are always present in the process of computations, although they will remain definite by the condition (3.18). It is well-known that these errors will be lessened by the smoothing. The total energy of the vibrating media is diminished by this smoothing pro-

cess, meanwhile the energy is actually diminished through the action of lateral mixing which is not considered in above computations.

We now notice to diffusion equations of the type

$$\frac{\partial s_x'}{\partial t}=\mu\left(\frac{\partial^2 s_x'}{\partial x^2}+\frac{\partial^2 s_x'}{\partial y^2}\right), \tag{3.19}$$

or

$$s_x'(x, y, t+\Delta t')=s_x'(x, y, t)+\frac{\mu\Delta t'}{4(\Delta s)^2}\{s_x'(x+2\Delta s, y, t)+ +s_x'(x-2\Delta s, y, t)+s_x'(x, y+2\Delta s, t)+s_x'(x, y-2\Delta s, t) -4s'_x, (x, y, t)\}, \tag{3.20}$$

where μ is the lateral mixing coefficent, and $\Delta t'$ is the time step in this computation.

From (3.20) it is easily shown that tihis also represents the smoothing prcess. Therefore, the rate of the energy loss in the smoothing process will coincide with that resulted from the lateral mixing, provided that we make use the diffusion equations of the type (3.19) or (3.20).

We shall take $\Delta t=1200$ (sec), and $\frac{\mu\Delta t'}{4(\Delta s)^2}=0.01$ in the following computations. This means that the smoothing is made at every 20 minutes, and $\mu=1.3\times10^6$ c.g.s. in Ise Bay, and $\mu=0.6\times10^6$ c.g.s. in Tokyo Bay, respectively.

3.3. Procedure of programing

The main procedure of programing is as follows.

(i). *Input of the data.* The constants of typhoon, its initial location, and its movement are first to be read in. The water depth distribution of the bay, and the designation for the output data are also included here.

(ii). *Making the tables of hydrostatic surface elevations and gradient wind.* They are computed before the step by step computations as the functions of the distances from the typhoon center The tables are then stored in the core memories.

(iii). *Giving the initial values.*

(iv). *Computations of ζ_0 and Wg (gradient wind speed).* They are computed at each mesh point before each 20-minutes steps, where the distances from the typhoon center are computed for the central time of these steps.

(v). *Computations of ζ, s_x' and s_y' for each step.* The computations are made according to the equations (3.14) from the mouth to the bottom of the bay.

(vi). *Smoothing.* This is made after every 20-minutes steps. Equations of the type (3.20) are used for this purpose.

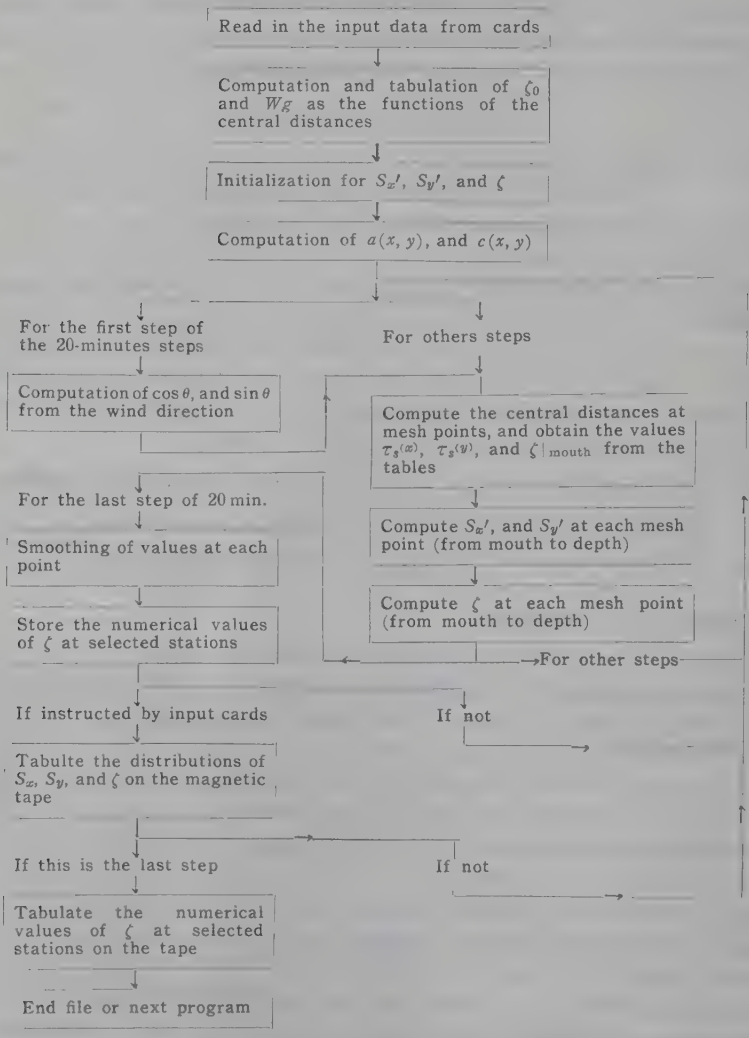
Read in the input data from cards
Computation and tabulation of ζ_0 and Wg as the functions of the central distances
Initialization for S_x', S_y', and ζ
Computation of $a(x, y)$, and $c(x, y)$
For the first step of the 20-minutes steps
For others steps
Computation of $\cos\theta$, and $\sin\theta$ from the wind direction
Compute the central distances at mesh points, and obtain the values $\tau_s^{(x)}$, $\tau_s^{(y)}$, and $\zeta|_{\text{mouth}}$ from the tables
For the last step of 20 min.
Compute S_x', and S_y' at each mesh point (from mouth to depth)
Smoothing of values at each point
Compute ζ at each mesh point (from mouth to depth)
Store the numerical values of ζ at selected stations
For other steps
If instructed by input cards
If not
Tabulte the distributions of S_x, S_y, and ζ on the magnetic tape
If this is the last step
If not
Tabulate the numerical values of ζ at selected stations on the tape
End file or next program

Fig. 3.2. Flow chart of the first program of storm-surge computation for Ise Bay.

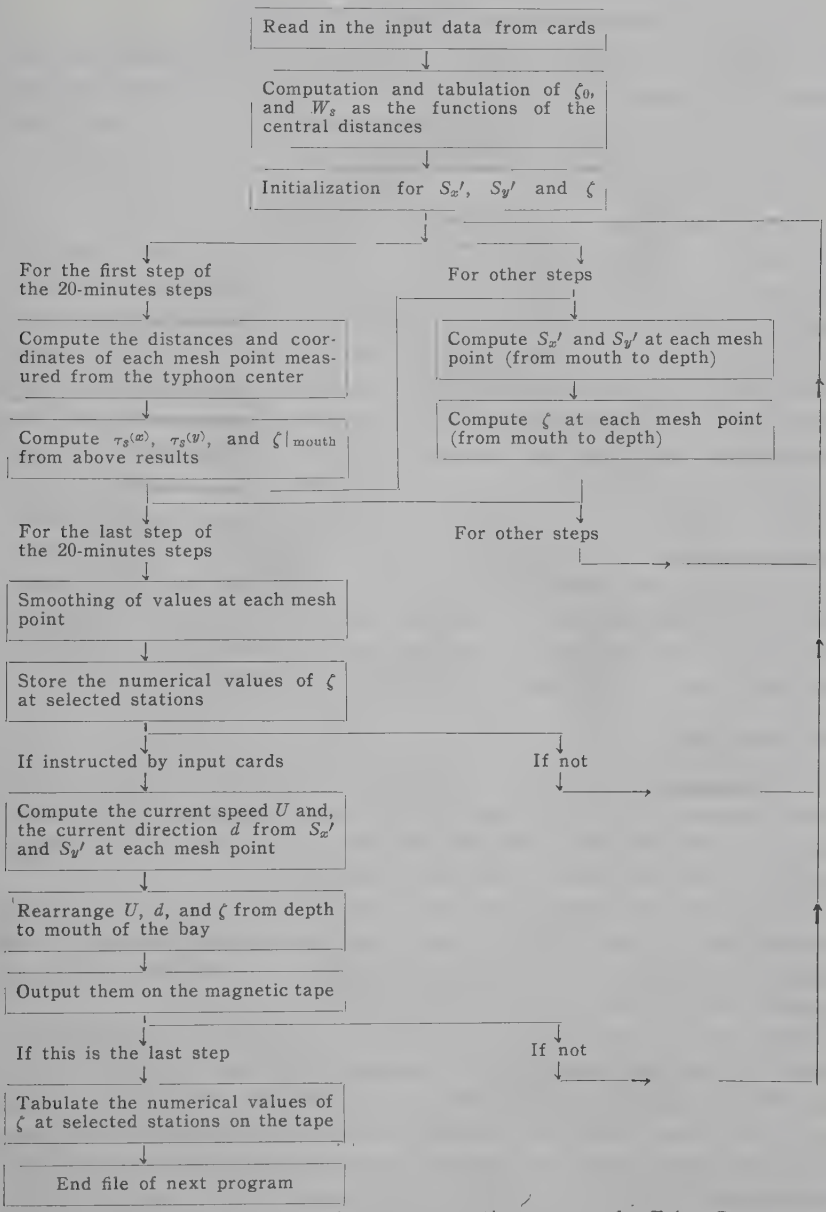
Read in the input data from cards
Computation and tabulation of ζ_0, and W_s as the functions of the central distances
Initialization for S_x', S_y' and ζ
For the first step of the 20-minutes steps
For other steps
Compute the distances and coordinates of each mesh point measured from the typhoon center
Compute S_x' and S_y' at each mesh point (from mouth to depth)
Compute $\tau_s^{(x)}$, $\tau_s^{(y)}$, and $\zeta|_{\text{mouth}}$ from above results
Compute ζ at each mesh point (from mouth to depth)
For the last step of the 20-minutes steps
For other steps
Smoothing of values at each mesh point
Store the numerical values of ζ at selected stations
If instructed by input cards
If not
Compute the current speed U and, the current direction d from S_x' and S_y' at each mesh point
Rearrange U, d, and ζ from depth to mouth of the bay
Output them on the magnetic tape
If this is the last step
If not
Tabulate the numerical values of ζ at selected stations on the tape
End file of next program

Fig. 3.3· Flow chart of the surge-computing program for Tokyo Bay.

(vii). *Arrangement of the output data.* The output data are arranged here according to the programed design. At each 20-minutes step, we can tabulate ζ values at selected stations, and the distributions of ζ, u (or S_x), and V (or S_y). The selected stations, and the choise of output steps are first designed by input cards.

Fig. 3.2 and 3.3 are the examples of flow chart for the coses of Ise Bay and Tokyo Bay, respectively. For the case of Ise Bay, we made more than 3 programs in the first program of them (Fig. 3.2), we assumed that the wind direction is the function of time only, and neglected the bottom stress. In the second, we assumed the linear dependence of the flow to the bottom stress. In the third, we assumed that the wind in the typhoon area consisted of two parts, the field wind and the wind proportional to the gradient wind, the bottom stress assumption being similar to that in the second program. In these programs, we supposed that the vertical eddy viscosity was constant.

For the case of Tokyo Bay (Fig. 3.3), the wind distribution and the bottom stress are supposed to be similar as those in the third program for Ise Bay, but the vertical eddy viscosity is assumed to be proportional to the water depth. The elevations were not neglected against the water depth in this case. This program was also applied to Ise Bay, where the branch bays, Chita Bay and Atsumi Bay, were disregarded to simplify the problem.

3.4. Computations for Ise Bay

On September 26, 1959, a severe typhoon struck the coast of Ise Bay (including Nagoya City), and its neighborhood. Huge storm surges were produced in this bay, and more than 5,000 lives were lost at that time. This typhoon was lately called by the name 'Ise Bay Typhoon'.

At Nagoya, the maximum sea level was 3.89 m higher than T.P. or the standard mean sea level of Tokyo Bay. The corresponding departure from normal is 3.4 m, which is the highest recorded value of storm surges along the coast of Japan.

We made the computations of these surges by using these four programs. Three of them were made by three programs of Ise Bay, respectively. The last one was made by using the program for Tokyo Bay, which is expressed later. The whole area was considered in the first three cases, but only Ise Bay in the narrow sense was considered in the last case, as we already mentioned above.

Fig. 3.4. Ise Bay and its neighborhood.

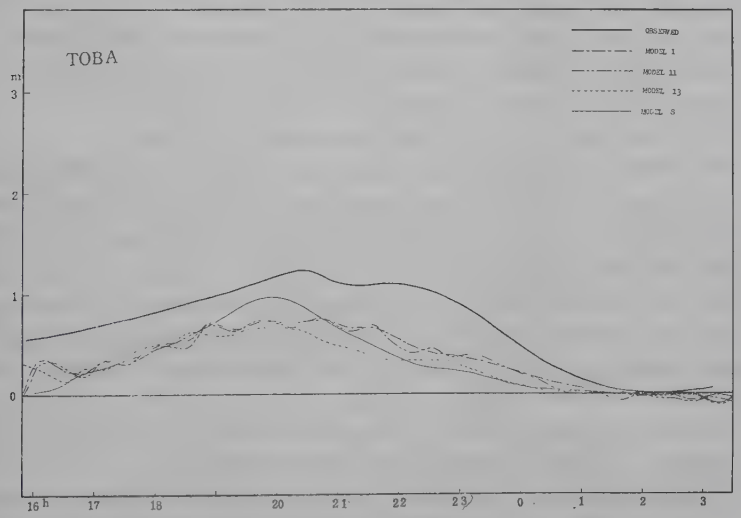

Fig. 3.5. Observed and computed variations of storm surges at Toba.

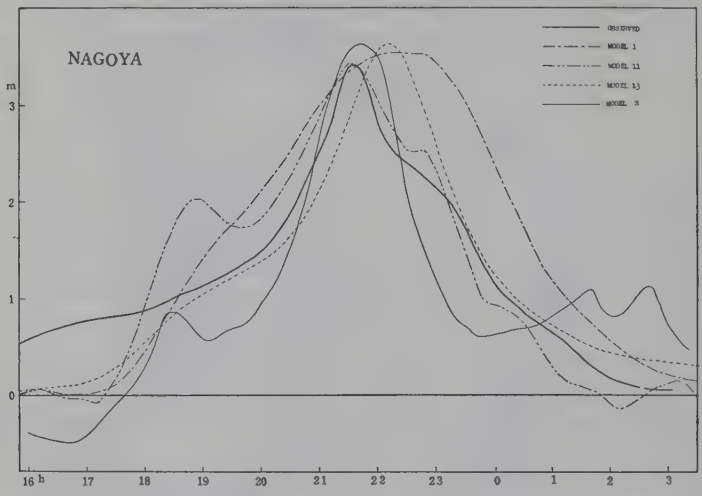

Fig. 3.6. Observed and computed variations of storm surges at Nagoya.

Computed timely variations of storm surges are plotted in Fig. 3.5—3.7 at three selected stations, Taba, Nagoya, and Maeshiba, for these four medels. In these stations, Toba is situated near the mouth of Ise Bay, Nagoya near the bottom of it, and Maeshiba near the bottom of a brach bay, Atsumi Bay, and about 70 km southeast of Nagoya.

From these figures, the following conclusions will be given.

(i). The computed values are generally in agreement with the observed ones.

(ii). The surge heights are in good agreement with the observations at Nagoya and Maeshiba, but the former is fairly smaller than the latter at Toba, which is situated near the mouth.

(iii). In the first three models, the computed phases of maximum surges agree well with the observed ones when we disregard the bottom stress, but the computed phases lag from the observed ones when we take the bottom stress into account.

(iv). However, in the last model, the computed phases fairly resemble to the observations under the existence of the bottom stress.

(v). The seiches are too remarkable when we disregard the bottom stress.

(vi). The computed patterns of storm surge variations seem to be more realistic

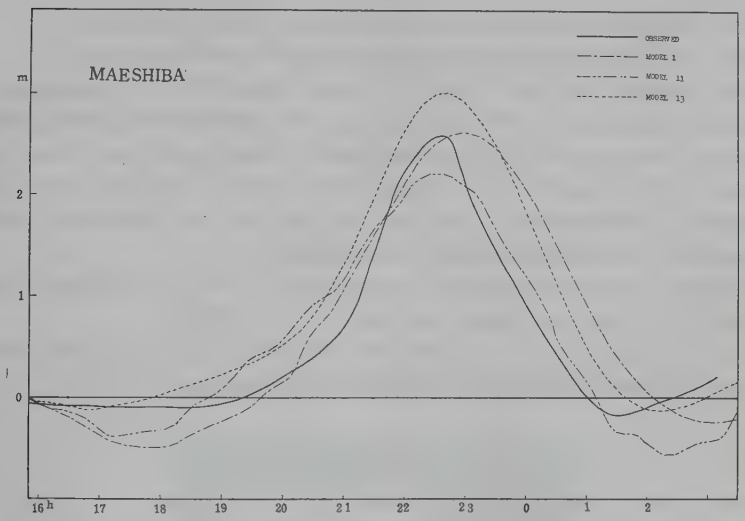

Fig. 3.7. Observed and computed variations of storm surges at Maeshiba.

Assumptions for each model

Model	Bottom stress	Wind assumption
11	absent	direction is the function of time only
1	present	〃
13	present	wind consists of two parts
15	present (proportional to the current speed square)	〃

in the third and forth models than those in the second model.

Main characteristics of computed results in these four models will be sketched in above conclusions. We feel from them that the assumption of constant eddy viscosity will give too large frictional effects in shallow waters, especially in the period of the nearest typhoon approach. The phase and height of maximum surge will fairly resemble to the observations when we neglect the bottom stress. However, in this case, the computed pattern is discrepant from the observed one especially in the later periods.

3.5. Computations for Tokyo Bay

One of the most destructive storm surges in Tokyo Bay was that on October 1, 1917, which was produced by a severe typhoon (see Table 2.1). We

had few tide-guage records at that time, and the exact estimations of storm surges in Tokyo Bay were only possible at few river-side stations.

The maximum sea level was 3.79 m higher than T.P. at Komatsugawa in Tokyo, near the mouth of Riv. Nakagawa. The corresponding surge height is 1.90 m, according to our new estimation. More higher values were also reported at other stations (for instance 2.3 m at Horie, situated about 4 km southeast of Komatsugawa), but they will be not exact estimations as the corresponding tide predictions were all insufficient.

Destructive storm surges were also produced in 1911 by a typhoon of similar track. The maximum surge was then 1.3 m at Tokyo.

Above-metioned surges were produced by typhoons whose tracks were nearly parallel to the axis of Tokyo Bay. One of other dangerous tracks of typhoons

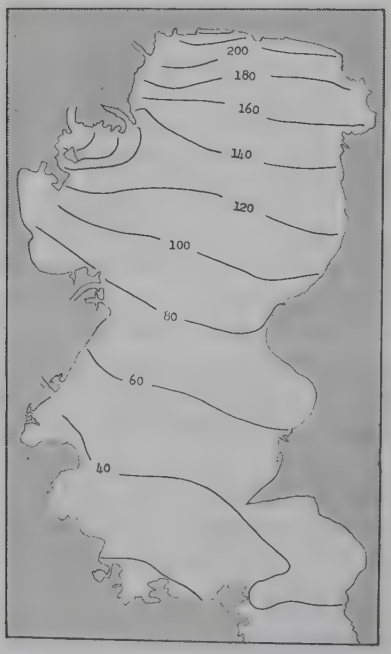

Fig. 3.8. Horizontal distribution of surges immediately after the nearest approach of 1917-typhoon to Tokyo (4 h, October 1).

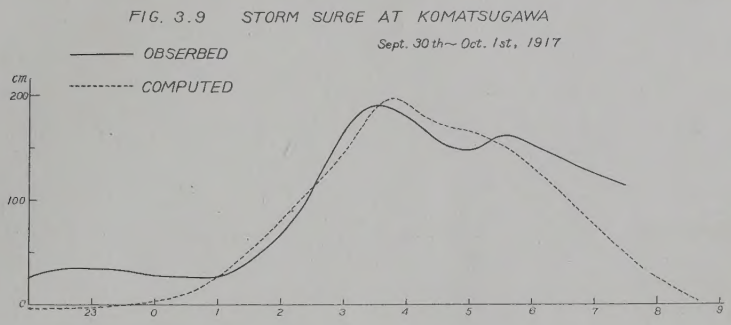

Fig. 3.9. Storm surge at Komatsugawa (Sept. 30th~Oct. 1st, 1917)

will be that of the Kitty Typhoon in 1949, whose track was from south to north (see Table 2.1). This typhoon was not so powerful, and the maximum surge was only 1.41 m at Tsukiji, Tokyo. Howerer, more destructive surges are expected by more powerful typhoons of similar tracks.

We have computed the numerical surge patterns in Tokyo Bay for several cases according to the last program in the preceding paragrgph (see Fig. 3.3), where the above.mentioned typhoons and the Ise Bay Typhoon were taken into account. Fig. 3.8 shows the computed horizontal patterns of 1917-surges near the maximum time. The maximum value is about 2.6 m at the bottom of the Bay. The maximum value becomes about 3.0 m if we take the Ise Bay Typhoon instead of the 1917-typhoon, which is about one half meters lower than the corresponding value in Ise Bay.

The computed timely variations at Komatsugawa are shown in Fig. 3.9 by the solid (computed) and dotted (observed) curves. Fig. 3.9 shows that the computation is in good agreement with the observation at this station.

We also computed the cases where the same typhoon took the track of the Kitty Typhoon, and the maximum computed surges were 10—30 cm higher than the former case near Tokyo, although they are fairly lowever than the former near the bottom of the Bay. The similar results are also shown in the cases of other typhoon models.

(to be continued)

昭和36年11月5日印刷
昭和36年11月10日発行

編集兼発行人　気象庁
東京都千代田区大手町一ノ七

印刷者　花崎実
東京都中央区新富町二ノ十九

印刷所　大東印刷工芸株式会社
東京都中央区新富町二ノ十九